Imperial College London
Department of Earth Science and Engineering

Modelling ice-ocean interactions in and around ice shelves

James R. Jordan

May 2015

Supervised by Matthew Piggott, Paul Holland and Adrian Jenkins

Submitted in part fulfilment of the requirements for the degree of
Doctor of Philosophy in Earth Science and Engineering of Imperial College London
and the Diploma of Imperial College London

Abstract

Physical processes in Antarctica and the Southern Ocean are of great importance to the global climate system. This thesis considers two such processes, namely ice-ocean interaction in ice shelf basal crevasses and the conditional instability of frazil ice growth.

It has been suggested that freezing within basal crevasses can act as a stabilising influence on ice shelves, preventing their break up. Using Fluidity, a finite element ocean model, it is found that ocean circulation within a crevasse is highly dependent upon the amount of freezing in the crevasse. It is also found that frazil ice formation is responsible for the vast majority of freezing within a crevasse, and that there is a non linear relationship between the amount of supercooling in a crevasse and its freeze rate.

The conditional instability of frazil ice growth is a little investigated mechanism of ice growth. Any frazil forming in the water column reduces the bulk density of a parcel of frazil-seawater mixture, causing it to rise. Due to the pressure-decrease in the freezing point, this causes more frazil to form, causing the parcel to accelerate, and so on. Numerical modelling finds that the instability does not operate in the presence of strong stratification, high thermal driving (warm water), a small initial perturbation, high 'background' mixing or the prevalence of large frazil ice crystals. Given a large enough initial perturbation this instability could allow significant rates of ice growth even in water that is above the freezing point.

The research presented in this thesis forms the material for two peer-reviewed publications; 'Modelling ice ocean interactions in ice shelf basal crevasses' (*Jordan et al.*, 2014) and 'On the conditional frazil ice instability in seawater' (*Jordan et al.*, 2015)

Copyright license

The copyright of this thesis rests with the author and is made available under a Creative Commons Attribution Non-Commercial No Derivatives licence. Researchers are free to copy, distribute or transmit the thesis on the condition that they attribute it, that they do not use it for commercial purposes and that they do not alter, transform or build upon it. For any reuse or redistribution, researchers must make clear to others the licence terms of this work.

Declaration

I hereby certify that any use of material in this thesis that is not my own has been properly acknowledged.

No part of this thesis has been submitted in support of another degree at Imperial College London, or anywhere else.

James Rowan Jordan

May, 2015

There are many people who have made the last three and bit years at BAS such an enjoyable and rewarding part of my life, and as such are deserving of thanks. They are, in no particular order, the scientists and crew of the JCR GENTOO 2012 cruise to the Weddel sea, the Cambridge crew of Nicola, Phil and Adele, Mum, Dad and my borther Tom,BAS students past and present (in particular Sarah, Jen, Finn and Tommy for putting up with sharing an office with me), my house-mates Martin, Ashleigh, Vicky and Tom (for likewise putting up with sharing a house with me during the more stressful parts of the last few years) and my supervisors Paul, Matt and Adrian. Paul deserves a special thanks for helping to turn my gibberish into (hopefully) legible text. And finally, I'd like to thank anyone who is reading this; after spending so long working on this project it's good to think that other people may take an interest in the work I've been doing over the last several years.

Contents

1 Introduction **16**

1.1 Aim of the Thesis . . . 16

1.2 Antarctica and the Southern Ocean . . . 17

1.2.1 Thermohaline circulation . . . 17

1.3 Ice shelves . . . 20

1.3.1 Sea level rise . . . 21

1.3.2 Ice shelf stability . . . 21

1.4 Types of ice . . . 25

1.5 Basal Crevasses . . . 26

1.6 Conditional instability of frazil ice . . . 32

1.7 Overview of the Thesis . . . 36

2 Model and governing equations **38**

2.1 Governing Equations . . . 38

2.2 Frazil ice model . . . 41

2.2.1 Frazil ice dynamics . . . 41

2.2.2 Frazil ice thermodynamics . . . 44

2.2.3 Implementation of frazil ice model in fluidity . . . 46

2.2.4 Validation of frazil model . . . 47

2.3 Ice shelf melt model . . . 50

3 Modelling ice-ocean interaction in idealised ice shelf basal crevasses **52**

3.1 Overview . . . 52

3.2 Model set-up . . . 53

3.2.1 Model calibration . . . 54

3.3 Base case . . . 58

3.4 Sensitivity study . . . 62

3.4.1 Temperature variation . . . 62

3.4.2 Velocity variation . . . 64

3.4.3 Frazil crystal size variation . . . 65

3.4.4 Crevasse geometry variation 66
3.5 Triangular crevasses 73
3.5.1 Long term ocean stabilisation of crevasses 73
3.6 Conclusions 78

4 The conditional instability of frazil ice in seawater 80
4.1 Overview 80
4.2 Numerical modelling of an idealised instability 81
4.2.1 Model setup 81
4.2.2 Results 84
4.3 Numerical modelling of an Ice Shelf Water outflow 95
4.3.1 Model setup 95
4.3.2 Results 98
4.4 Conclusions 104

5 Conclusions 106
5.1 Future Work 108

Bibliography 110

List of Tables

3.1 Average freezing rate and frazil ice contribution to freezing rate for the baseline, T2 (warmer than baseline), T3 (colder than baseline), R025 (smaller radii than baseline, R150 (larger radii than baseline). Freezing rates are spatially averaged over the top of the crevasse. . . . 63
3.2 The effect of far field temperature on freeze rate. 64
3.3 The effect of temperature variation on melt ratio. 75
3.4 The effect of inflow velocity variation on melt ratio. 75
3.5 The effect of crevasse depth on melt ratio. 75
3.6 The effect of crevasse width on melt ratio. 76

List of Figures

1.1 Map of Antarctica and the Southern Ocean. Image is sourced from http://www.geology.com. 18
1.2 Schematic diagram of the global thermohaline circulation. Warm water is transported poleward from the equator, before cooling and returning at depth. Image is sourced from http://www.ncdc.noaa.gov. 19
1.3 Ice thickness (m) for all Antarctic ice shelves. Adapted from *Griggs and Bamber* (2011). 23
1.4 Collapse of the Larsen B ice shelf, January–March 2002. Image sourced from NASA Earth Observatory. 24
1.5 Schematic diagram of the thermohaline circulation under an ice shelf (*Holland and Feltham*, 2005). The formation of sea ice generates High-Salinity Shelf Water, which sinks down the continental shelf and melts the ice shelf at its grounding line. The fresh meltwater released initiates an Ice Shelf Water plume, which becomes supercooled as it rises due to the pressure release and thus deposits ice at shallower depths. 24
1.6 (a) 25 MHz radar profile across basal and surface crevasses. Surface elevations have been corrected to reflect ice shelf topography. Note down warping of firn above basal crevasse and hyperbolas on the flanks, highlighted in red, interpreted as surface crevasses. (b) Three-dimensional view of the basal crevasse penetrating into the ice shelf. Surface and basal interface interpolated from GPS and GPR profiles, respectively. Figure sourced from *McGrath et al.* (2012a) 29

1.7 The profile of the rifts wall after a 25-year integration and at the end of a 50-year standard experiment compared with the initial wall location (which is represented by the vertical dotted line at the middle of the horizontal axis). The horizontal extensions of the two curves at the top indicate the interface between the accumulated ice and the water at the corresponding times. Over time the ice-ocean interface changes from vertical to sloping, driven by melting lower down in the water column and freezing higher up. Notice that the horizontal distance scale is exaggerated relative to the vertical one. Figure sourced from *Khazendar and Jenkins* (2003) 30

1.8 (a) 1986 Landsat image of LBIS (*Sievers et al.*, 1989) and (b) 2003–2004 MOA image of LCIS *Scambos et al.* (2007), both with 97–98 survey data. Red and (overlain) blue points mark surface and basal returns, so visible red points indicate failure to detect the base. Yellow shading indicates proposed marine ice and yellow tracks are other surveys incorporated in the ice draft. Figure sourced from *Holland et al.* (2009) 31

1.9 Schematic of frazil ice instability in an ISW plume. 35

2.1 Validation of frazil ice model. Modelled change in (a) thermal driving, (b) temperature, (c) salinity and (d) amount of frazil ice in a 1 m^2 box of water at sea level cooled by 0.1 °C is shown for r=0.25 mm (blue), r=0.75 mm (black) and r=1.25 mm (red). 49

3.1 Model mesh. Resolution varies from 5 m inside the basal crevasse to 20 m outside. A flow past the crevasse is imposed from left to right. . 56

3.2 Model calibration. The modelled calibration profiles of salinity and temperature are shown in black, with comparison profiles shown in green and observations shown in red (*Orheim et al.*, 1990; *Khazendar and Jenkins*, 2003). The freezing point of the inflow water is shown in blue. 56

3.3 (a) Maximum frazil ice production, (b) maximum supercooling, (c) maximum velocity magnitude in the crevasse and (d) maximum ice shelf melt rate for the baseline/calibration case. 57

3.4 Overview of ocean dynamics for the whole domain in the baseline case. Flow enters from the left and leaves via the right. Meltwater rises into the crevasse and freezes on the top, creating a cold and saline dense layer. This dense layer enhances the overturning circulation within the crevasse. 60
3.5 Baseline case showing (a) time-averaged mean density with mean velocity vectors, (b) mean temperature (colours) with mean thermal driving (contours), (c) mean frazil crystal production and (d) change in crevasse geometry as a result of mean melt rate maintained for 5 years with the position of the calibration and comparison profile shown in black and green respectively. The white contour in panel b is at zero thermal driving while black contours are every 0.1 degree above and black dashed contours are every 0.01 degree below this point. The pressure dependent freezing point (FP) of the water properties used for initial and inflow conditions is also shown. 61
3.6 Mean density with mean velocity vectors for the inflow temperatures (a) T1, (b) T2, (c) T3 (baseline) and (d) T4. The pressure dependent freezing point (FP) of the four different inflow temperatures is also shown. 67
3.7 Mean temperature (colours) with thermal driving (contours) for the inflow temperatures (a) T1, (b) T2, (c) T3 and (d) T4. The white contour is at thermal driving equal to 0, while black contours are every 0.1 degree above and black dashed contours are every 0.01 degree below this point. 68
3.8 Change in crevasse geometry as a result of averaged melt rate maintained for 10 years for (a) temperature variation of inflow water, (b) velocity variation of inflow water, (c) variation in frazil crystal radii and (d) effect of no frazil component in the model. An increase in crevasse size represents melting whilst a decrease represents freezing. 69
3.9 Time averaged mean density with time averaged mean velocity vectors for (a) the no-melting case, (b) the no-frazil case, (c) R025, (d) R075 (baseline) and (e) R150. 70

3.10 Mean temperature (colours) with thermal driving (contours) for (a) the no-frazil case, (b) R025, (c) R075 (baseline), (d) R150. The white contour is at thermal driving equal to 0, while black contours are every 0.1 degree above and black dashed contours are every 0.01 degree below this point. 71
3.11 Mean density with mean velocity vectors for different crevasse geometries (a) 260 m wide and 170 m deep, (b) 130 m wide and 340 m deep, (c) cavity extended to 200 m deep and (d) cavity extended to 500 m deep. 72
3.12 Triangular crevasse with the same set up parameters as the baseline case showing (a) time-averaged mean density with mean velocity vectors, (b) mean temperature (colours) with mean thermal driving (contours), (c) mean frazil crystal production and (d) change in crevasse geometry as a result of mean melt rate maintained for 5 years. The white contour in panel b is at zero thermal driving while black contours are every 0.1 degree above and black dashed contours are every 0.01 degree below this point. The pressure dependent freezing point (FP) of the water properties used for initial and inflow conditions is also shown. 76
3.13 Definition of melt ratio. The melt ratio is equal to the mean melt rate of the inside walls of the crevasse in the direction perpendicular to the wall (A) divided by the mean melt rate of the outside the of the crevasse (B). 77

4.1 Idealised non-hydrostatic ocean model setup. Initial profiles for the baseline case (T^*_{in}=10^{-1} °C, $\frac{\partial \rho}{\partial z}_{in} = -10^{-5}$ kg m^{-4}, $C_{in} = 10^{-3}$, $r =$ 0.75 mm and $K = 10^{-3}$ m^2 s^{-1}) of (a) T (black) and T_F (blue), (b) S and (c) C. 83
4.2 Results of the idealised non-hydrostatic ocean model setup. The instability for the unstable baseline case (T^*_{in}=10^{-1} °C, $\frac{\partial \rho}{\partial z}_{in} = -10^{-5}$ kg m^{-4}, $C_{in} = 10^{-3}$, $r = 0.75$ mm and $K = 10^{-3}$ m^2 s^{-1}) in terms of (a) density relative to initial density, (b) thermal driving, (c) salinity relative to initial salinity and (d) frazil ice concentration. 85

4.3 Results of the idealised non-hydrostatic ocean model setup. Panels show the density relative to the initial density of (a) the baseline case (T^*_{in}=10^{-1} °C, $\frac{\partial\rho}{\partial z}_{in} = -10^{-5}$ kg m^{-4}, $C_{in} = 10^{-3}$, $r = 0.75$ mm and $K = 10^{-3}$ m^2 s^{-1}) and also cases for which the instability is limited by (b) stratification ($\frac{\partial\rho}{\partial z}_{in} = -10^{-3}$), (c) thermal driving ($T^*_{in}$=1°C), (d) background mixing ($K = 10^{-1}$ m^2 s^{-1}) and (e) salinity compensated case where the salinity in the bottom 20 m has been increased by an amount equal to melting the initial frazil ice concentration. Note the different time axes. 87

4.4 Results of the idealised non-hydrostatic ocean model setup. The instability for the purely thermally stable case (T^*_{in}=1°C, $\frac{\partial\rho}{\partial z}_{in} = -10^{-5}$ kg m^{-4}, $C_{in} = 10^{-3}$, $r = 0.75$ mm and $K = 10^{-3}$ m^2 s^{-1} with salinity in the bottom 20 m reduced to compensate the 1°C warming of the rest of the domain) in terms of (a) density of the combined frazil-seawater mixture relative to the initial density, (b) thermal driving, (c) salinity relative to initial salinity and (d) frazil ice concentration. . 89

4.5 Total frazil ice at the end of the idealised non-hydrostatic ocean model simulation as a function of thermal driving and density gradient for C_{in}=10^{-3}, r=0.75 mm and $K = 10^{-3}$ m^2 s^{-1}. Model runs were carried out for the 18 combinations of T^*_{in} and $\frac{\partial\rho}{\partial z}_{in}$ marked in white, with results linearly interpolated between. The white contour shows where the initial frazil ice concentration is the same as the final frazil ice concentration (note logarithmic scale). The final locations of the (a) the baseline, (b) the stratification-limited cases and (c) the thermal-driving limited shown in Fig. 4.3 are marked. 91

4.6 Evolution of total frazil ice in the idealised non-hydrostatic ocean model for (a) the full 20000 s of the model run and (b) the first 2500 s. The baseline case (T^*_{in}=10^{-1} °C, $\frac{\partial\rho}{\partial z}_{in} = -10^{-5}$ kg m^{-4}, $C_{in} = 10^{-3}$, $r = 0.75$ mm and $K = 10^{-3}$ m^2 s^{-1}) is shown, and the black dashed line shows the amount of frazil ice at the start of the simulation. Also shown are the results of varying higher and lower temperatures (T^*_{in} = 1 °C, $T^*_{in} = 10^{-2}$ °C), stratification ($\frac{\partial\rho}{\partial z}_{in} = -10^{-3}$ kg m^{-4}, $\frac{\partial\rho}{\partial z}_{in} = -10^{-6}$ kg m^{-4}), frazil crystal radius ($r = 0.125$ mm, r= 0.25 mm), K (10^{-1} m^2 s^{-1},10^{-5} m^2 s^{-1}) C_{in}, initial frazil concentration (C_{in}= 2×10^{-3} and C_{in}= 5×10^{-2}), salinity compensated case (where salinity in the bottom 20 m has been increased to directly offset the freshwater anomaly gained from melting the initial frazil ice concentration), pure thermally stableaised case (where salinity in the bottom 20 m has been reduced to off set the density change arise from the increase in thermal driving of the rest of the domain) and frazil rise velocity (w_i = 0 m s^{-1}) whilst keeping all other parameters at their baseline values. 93

4.7 Schematic of non-hydrostatic ice-shelf model setup. An inflow enters the domain from the bottom 100 m on the right-hand side and leaves via the bottom 100 m on the right-hand side. The inflow water is at the freezing temperature, whilst the rest of the domain has a constant thermal driving. No frazil is present in the inflow or initial conditions. 97

4.8 Evolution of frazil ice growth in the non-hydrostatic ice shelf model for the baseline case (T^*_{in}=10^{-2} °C, $\frac{\partial\rho}{\partial z}_{in} = -10^{-6}$ kg m^{-4}, $r = 0.75$ mm and $K = 10^{-3}$ m^2 s^{-1}) in terms of (a) density relative to initial density, (b) thermal driving, (c) salinity relative to initial salinity and (d) frazil ice concentration. 99

4.9 Results of the non-hydrostatic Ice Shelf Water model setup. Spatial mean frazil ice deposition after 24 hours as a function of thermal driving and density gradient for $r = 0.75$ mm and $K = 10^{-3}$ m^2 s^{-1}. Model runs were carried out for combinations of T^*_{in} and $\frac{\partial\rho}{\partial z}_{in}$ marked in white, with results linearly interpolated between. The white contour shows the zero deposition contour. The location of (a) the baseline case is shown. 101

4.10 Results of the non-hydrostatic Ice Shelf Water model setup. Sensitivity of frazil ice deposition after 24 hours to (a) thermal driving, (b) background mixing, (c) stratification,fff (d) frazil crystal radius, (e) inflow velocity and (f) time. In each case the baseline case is shown in black. 103

1 Introduction

1.1 Aim of the Thesis

The main aim of this thesis is to better understand some of the small scale ice-ocean interactions that happen in and around ice shelves in Antarctica. Large scale climate models tend to, by necessity, either ignore or simplify a lot of these processes. Two particular processes are investigated, namely ocean stabilising of ice shelves by freezing in basal crevasses and the conditional instability of frazil ice growth. Direct observations of these processes are difficult to obtain whilst laboratory experiments are impractical. Model simulations, therefore, provide the only practical way of studying these poorly understood processes. The work presented here is the first two-dimensional ocean modelling study of an individual ice shelf basal crevasse, as well as the first modelling study of the conditional instability of frazil ice. To achieve this Fluidity, a non-hydrostatic finite-element ocean model with a flexible unstructured mesh, is used. Whilst Fluidity is not an OGCM (oceanic general circulation model) it is well suited to the complex geometry and high vertical resolution needed to accurately model the ocean around ice shelves. In effect, Fluidity is used as a means of carrying out 'geophysical experiments' that would otherwise be impossible to do.

1.2 Antarctica and the Southern Ocean

The Intergovernmental Panel on Climate Change (IPCC) states that the observed 'Warming of the climate system is unequivocal', and that 'Ocean warming dominates the increase in energy stored in the climate system' (*IPCC*, 2013). However, this warming of the climate system is not uniform in space with places in Antarctica and the Southern Ocean being amongst those warming the quickest (*Bromwich et al.*, 2013). The Southern Ocean (Fig. 1.1) covers the immediate area around Antarctica. As it shares boundaries with the Pacific, Atlantic and Indian oceans, the Southern Ocean is of vital importance for global circulation and oceanic heat transport.

1.2.1 Thermohaline circulation

The thermohaline circulation is the an important mechanism by which heat is transported around the worlds ocean (*Bryan*, 1962; *Hall and Bryden*, 1982). Warm water from the equator is transported poleward via wind driven surface currents, where it cools, becomes denser and sinks. This dense water then returns towards the equator (Fig. 1.2). The strength of the thermohaline circulation is of vital importance for the global climate due to the oceanic mixing and global heat transport it provides.

Cold, dense Antarctic Bottom Water (AABW) is the densest observed water mass and is present in every ocean basin. It forms as a result of ice-ocean interaction around Antarctica. When new sea ice is formed on the continental shelf the remaining water becomes relatively more saline due to brine rejection and is then known as High Salinity Shelf Water (HSSW). The density of water at temperatures near the freezing point is determined mainly by its salinity, and so the water falls down the continental slope and out to the surrounding ocean basins where it becomes AABW.

Figure 1.1: Map of Antarctica and the Southern Ocean. Image is sourced from http://www.geology.com.

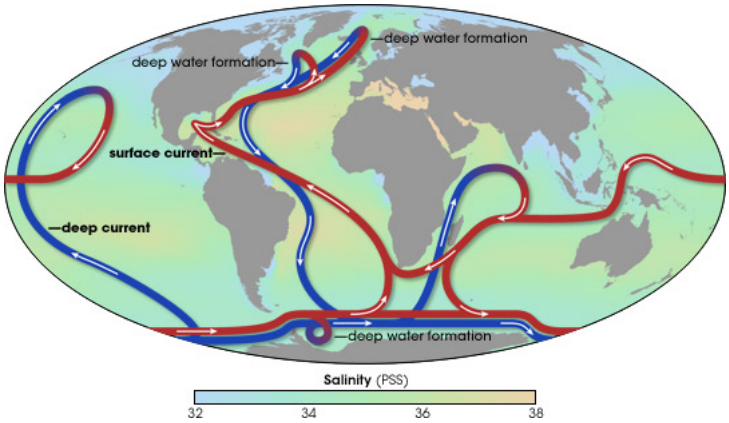

Figure 1.2: Schematic diagram of the global thermohaline circulation. Warm water is transported poleward from the equator, before cooling and returning at depth. Image is sourced from http://www.ncdc.noaa.gov.

1.3 Ice shelves

When Antarctic ice streams flow out over the ocean they form large floating ice shelves (*Pritchard et al.*, 2012; *Rignot et al.*, 2013). Ice shelves can be of the order of 100,000 km^2, with the largest being over 400,000 km^2. They vary in thickness, getting shallower as they approach the calving front but are typically several hundred metres thick (Fig. 1.3).

HSSW can enter the cavity beneath cold-water glacial ice shelves such as the Filchner-Ronne and Ross ice shelves (*Nicholls and Østerhus*, 2004; *Nicholls et al.*, 2009). The freezing temperature of seawater decreases with increasing pressure, and therefore the HSSW can melt the ice shelf at depth. The resulting meltwater cools and freshens the ambient seawater to form Ice Shelf Water (ISW), which is colder than the surface freezing point. The density of seawater is controlled by salinity near the freezing point, and therefore the fresher ISW is lighter than the surrounding seawater. When the ISW ascends along the ice shelf, it becomes supercooled and starts to freeze due to the increase in the local freezing temperature. This ascending ISW plume is important in determining the spatial patterns of melting and freezing beneath ice shelves (*Hellmer and Olbers*, 1989). The ascending ISW freezes both directly onto the ice shelf and through the formation of suspended frazil ice crystals. The buoyancy driving a plume is therefore a result of a mixed freshwater and frazil ice density perturbation. After ISW leaves the cavity, it contributes to the formation of AABW (*Foldvik et al.*, 2004).

Over the last few decades ice shelves on the Antarctic Peninsula have retreated, and this is thought to be associated with atmospheric warming (*Vaughan and Doake*, 1996). The most profound changes in the Antarctic Ice Sheet currently result from glacier dynamics at ocean margins, namely ice shelves (*Pritchard et al.*, 2009). The melting of the Antarctic Ice Sheet is predicted to have a large impact on global sea

level (*Shepherd et al.*, 2012).

1.3.1 Sea level rise

The stability of the Antarctic Ice Sheet is of great importance to future projections of global sea level rise, as it contains 70 % of the worlds freshwater. A total collapse and melting of the West Antarctic Ice Sheet would raise eustatic sea level by roughly 3.3 m (*Bamber et al.*, 2009), whilst the collapse of the much more stable East Antarctic Ice Sheet would raise sea level by around 50 m. Melting of sea ice and ice shelves has little direct input on sea level rise, as the ice is already displacing the amount of water that their melting would contribute to sea level rise. However, when ice shelves are thinning or collapse, the resulting reduction in buttressing of inshore glaciers can enhance the flow of outlet glaciers from the continental ice sheet and thus speed up the contribution of the ice sheets to sea level rise (*Rignot et al.*, 2004). These dramatic collapses are believed to be a result of thinning due to atmospheric warming and perhaps increased basal melting (*Shepherd et al.*, 2003; *Glasser and Scambos*, 2008; *Holland et al.*, 2011). As such a greater understanding of the factors that affect ice shelf stability is of importance for predicting future sea level rise and efforts to mitigate against coastal flooding.

1.3.2 Ice shelf stability

As well as a general reduction in Antarctic Peninsula ice shelf area (roughly 28,000 km^2 over the last 30 years (*Cook and Vaughan*, 2010)) there have been dramatic collapses of individual ice shelves over a short time period, such as Larsen A in 1995 and Larsen B in 2002. In the case of Larsen B an area of roughly 3250 km^2 disintegrated over a period of little more than 5 weeks in 2002 (Figure 1.4). The final collapse of these ice shelves was most likely a result of increased surface melt-

water production, leading to fracturing of the ice shelf into individual blocks of ice (*Scambos et al.*, 2000).

It is possible for the ocean to freeze onto the underside of ice shelves. Because the freezing temperature of seawater decreases with increasing pressure, water at the surface freezing point melts ice shelves at depth, generating meltwater, which is cooler and fresher than the surrounding water. The density of water at temperatures near the freezing point is determined mainly by its salinity, and therefore the meltwater is lighter than the surrounding water. As a result, the meltwater rises, and may become supercooled due to the pressure decrease (Figure 4.9) and form 'marine' ice on the base of the ice shelf (*Robin*, 1979). As well as direct freezing onto the ice base, small disc-shaped frazil ice crystals (with radii in the range 0.01–10 mm) form in a turbulent body of water when it becomes supercooled, and these can deposit on to the ice (*Daly*, 1984).

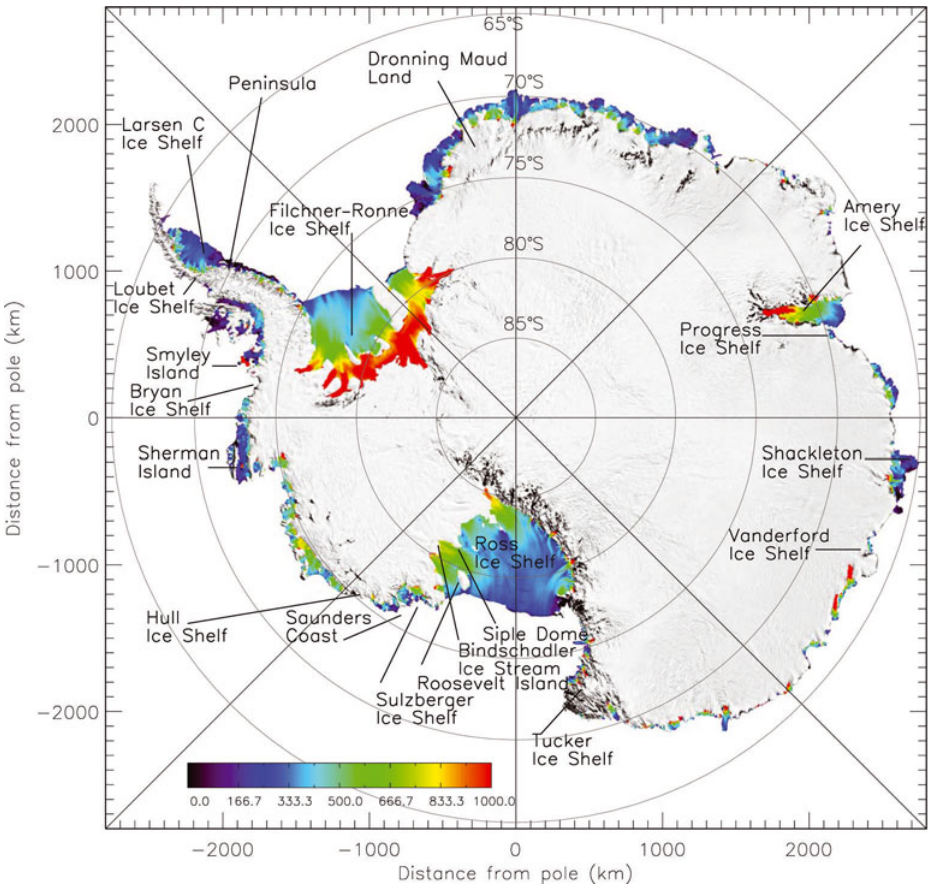

Figure 1.3: Ice thickness (m) for all Antarctic ice shelves. Adapted from *Griggs and Bamber* (2011).

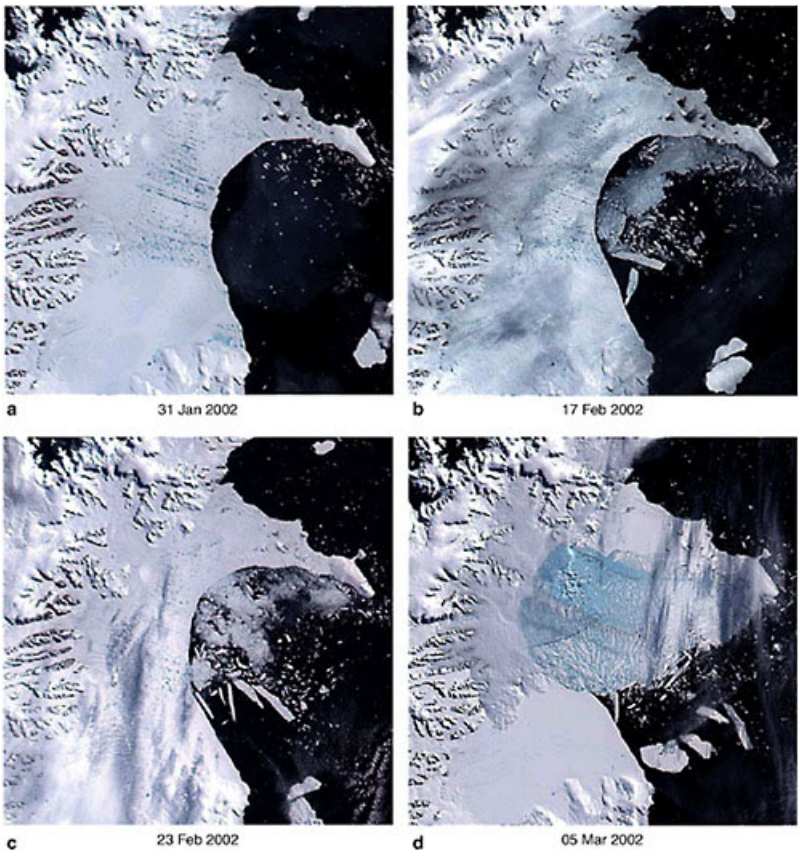

Figure 1.4: Collapse of the Larsen B ice shelf, January–March 2002. Image sourced from NASA Earth Observatory.

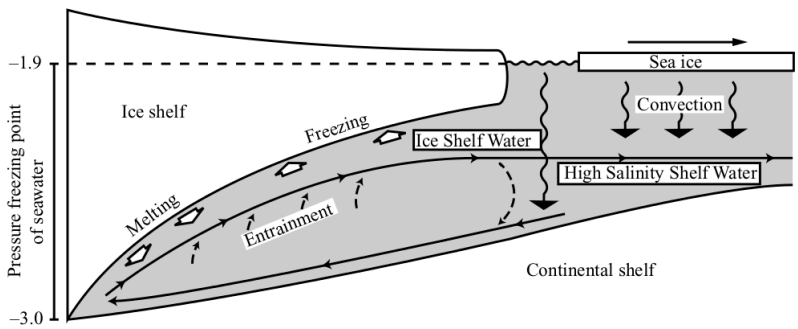

Figure 1.5: Schematic diagram of the thermohaline circulation under an ice shelf (*Holland and Feltham*, 2005). The formation of sea ice generates High-Salinity Shelf Water, which sinks down the continental shelf and melts the ice shelf at its grounding line. The fresh meltwater released initiates an Ice Shelf Water plume, which becomes supercooled as it rises due to the pressure release and thus deposits ice at shallower depths.

1.4 Types of ice

All types of ice formation in salty water act as a source of heat (due to the latent heat of ice fusion) and salt (due to brine rejection) in the water. Throughout this work several different types of ice are mentioned, namely meteoric ice, marine ice frazil ice and sea ice.

The Antarctic Ice Sheet is comprised of meteoric ice that has accumulated from thousands of years of precipitation. This ice is relatively cold, and as a result is brittle, with temperature determined by atmospheric conditions. Inland glaciers flows out towards the sea via ice streams, fast moving areas of the ice sheet that move at speeds of order 1 km a year. These ice streams flow out onto the sea, sometimes forming a floating ice shelf.

Marine ice is formed by the ocean freezing onto ice shelves. It is relatively warm, being formed at the freezing point of seawater (-2 ° C). As such it has a relatively low viscosity, and is more likely than meteoric ice to deform rather than fracture under stress. There is evidence to suggest that bands of marine ice act as a stabilising influence on ice shelves by halting the propagation of rifts (*Holland et al.*, 2009). Marine ice is a combination of direct ice growth and frazil ice deposition onto an ice surface.

Frazil ice is a collection of loose, randomly oriented disc-shaped ice crystals, formed in turbulent, supercooled water. The formation of frazil ice is a well known phenomenon in rivers and the uppermost layers of the ocean (*Martin*, 1981). There have also been observations at numerous Antarctic ice shelves of frazil ice up to several kilometres from the ice front, both suspended throughout the water column and present in sea ice cores (*Dieckmann et al.*, 1986; *Smetacek et al.*, 1992; *Penrose et al.*, 1994; *Leonard et al.*, 2006; *McGuinness et al.*, 2009; *Robinson et al.*, 2010).

The presence of ISW during the winter at McMurdo Sound has been linked to the growth of frazil ice on the underside of sea ice (*Mahoney et al.*, 2011), with up to 3 m of deposited frazil ice observed (*Robinson et al.*, 2014). There have also been observations of 6–7 m of frazil ice deposited on the underside of land fast sea ice *Price et al.* (2014).

Sea ice forms on the surface of oceans when the flow of heat from the ocean to the atmosphere results in the water becoming supercooled. Being so closely linked to atmospheric conditions results in a strong seasonal cycle in the extent of sea ice cover. Whilst both sea ice and marine ice are formed from oceanic freezing, within this work marine ice refers to ice frozen directly onto an ice shelf and sea ice refers to the seasonal sea-surface ice cover.

1.5 Basal Crevasses

Basal crevasses can form on the underside of ice shelves allowing seawater to penetrate the ice shelf and rupture the ice up to the level at which longitudinal stress acting to open the crevasse is sufficiently balanced by the confining presence of the surrounding ice (*Jezek*, 1984). An initial flaw in the base of the ice shelf will only propagate upwards if it exceeds a critical size, typically on the order of 1 m (*Rist et al.*, 2002). The final crevasses can be many kilometres long and several hundred metres wide and deep (*Luckman et al.*, 2012; *McGrath et al.*, 2012b,a). An example of a basal crevasse on the Larsen C Ice Shelf is shown in Fig. 1.6. Basal crevasses have been observed in detail on, among others, the Larsen (*Swithinbank*, 1977), Ross (*Jezek and Bentley*, 1983) and Fimbul (*Humbert and Steinhage*, 2011) ice shelves, and they are a common feature. Crevasses observed by *McGrath et al.* (2012b) were found to have their greatest depth and smallest width near their grounding line, with the crevasses becoming shallower and wider as they propagate towards the calving

front. *McGrath et al.* (2012b) suggest that this change in crevasse geometry is a combination of marine ice accretion at the top of the crevasse and bending stresses within the ice shelf, with the latter being the dominant process. This would lead to the formation of a melt-driven ocean convection cycle within the crevasse itself, with melting happening low down on the crevasse walls and marine ice accretion higher up (*Khazendar and Jenkins*, 2003).

The presence of basal crevasses will modify local stresses in the ice, potentially affecting ice shelf stability (*Jezek*, 1984; *Holland et al.*, 2009). They also increase the basal surface area over which melting occurs, and allow heat exchange between the ice and ocean deep within the ice column, potentially speeding up melting (*Hellmer and Jacobs*, 1992). Marine ice may form at the top of basal crevasses because the pressure freezing point difference between the base and top of the crevasse drives a thermohaline circulation within it. *Khazendar and Jenkins* (2003) modelled how this would cause a widening at the bottom of a crevasse and a narrowing at the top (Fig. 1.7).

Bands of marine ice, potentially formed in this way, have been observed in Larsen Ice Shelf, and this marine ice appears to play a role in stabilising the ice shelf (Fig. 1.8). Marine ice is comparatively warmer than meteoric ice and is therefore more likely to deform rather than fracture in response to stress. Marine ice has also been shown to heal rifts by binding their edges together with deformable material (*Rignot and MacAyeal*, 1998), and there is evidence that bands of marine ice act as a barrier to the propagation of rifts (*Holland et al.*, 2009). Airborne radar is able to get a strong return from an air-ice interface as well as a meteoric ice-ocean interface. When there is a marine ice-ocean interface, however, only a weak return is obtained. The absence of a radar echo from airborne radar can indicate the presence of marine ice, the exact thickness of which can be determined by the flotation depth of the ice shelf assuming hydrostatic equilibrium.

Obtaining observations of the physical conditions beneath ice shelves is challenging, and there are particularly few observations of ocean conditions within basal crevasses. Temperature and salinity profiles measured in the Jutulgryta rift, a 340 m wide and 260 m deep rift on the Fimbul Ice Shelf, were obtained by *Orheim et al.* (1990) (reprinted by *Khazendar and Jenkins* (2003)). A rift differs from a crevasse in that it extends vertically throughout the entire ice column, however as the Jutulgryta rift was "capped" by approximately 40 m of sea ice, marine ice and ice debris it is assumed to be a fair approximation to a basal crevasse. Ocean properties were vertically uniform within the rift, with a 60 m thick layer of supercooled water and frazil ice at the top. Approximately 2 m of ice accumulation occurred at the top of the rift over the course of two years (*Østerhus and Orheim*, 1992; *Khazendar and Jenkins*, 2003) and the average flow velocity past the crevasse was of the order of 2.5 cm s^{-1} (*Orheim et al.*, 1990).

Previous studies of ice shelf basal crevasses have mainly considered the formation and evolution of the crevasse itself rather than ocean flow and freezing within it (e.g. *Luckman et al.*, 2012; *McGrath et al.*, 2012b,a). Ocean modelling work has generally been at larger scales, considering ice shelf cavities as a whole rather than individual basal crevasses. (*Khazendar and Jenkins*, 2003) modelled in one (vertical) dimension the freezing rate within a basal crevasse and the impact this has on the water inside. However, the one-dimensional nature of their model limited the representation of ocean dynamics. As such there is there is a clear scope for a more in depth study of a process that is of great importance for ice shelf stability and hence global sea level rise.

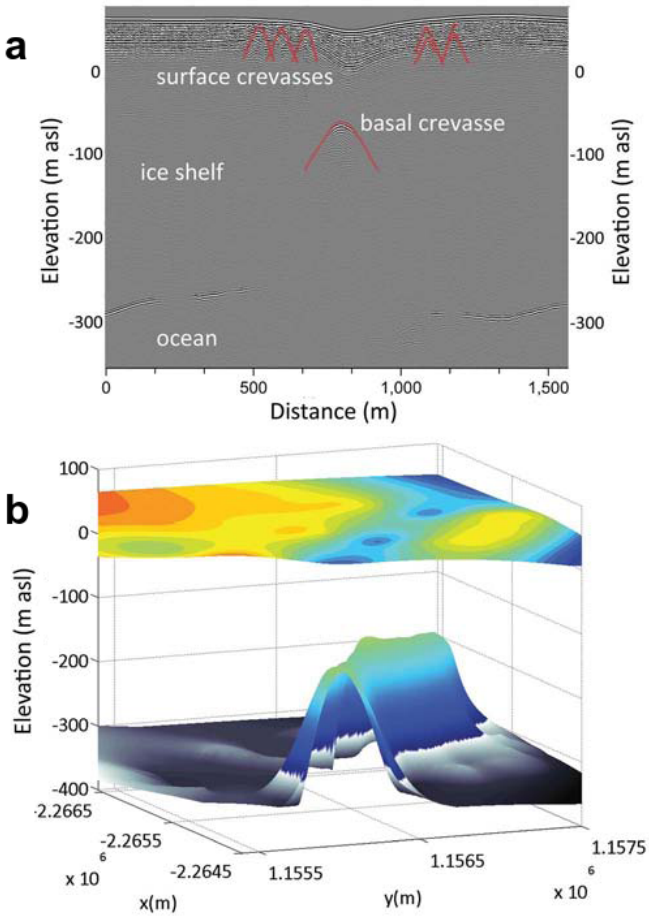

Figure 1.6: (a) 25 MHz radar profile across basal and surface crevasses. Surface elevations have been corrected to reflect ice shelf topography. Note down warping of firn above basal crevasse and hyperbolas on the flanks, highlighted in red, interpreted as surface crevasses. (b) Three-dimensional view of the basal crevasse penetrating into the ice shelf. Surface and basal interface interpolated from GPS and GPR profiles, respectively. Figure sourced from *McGrath et al.* (2012a)

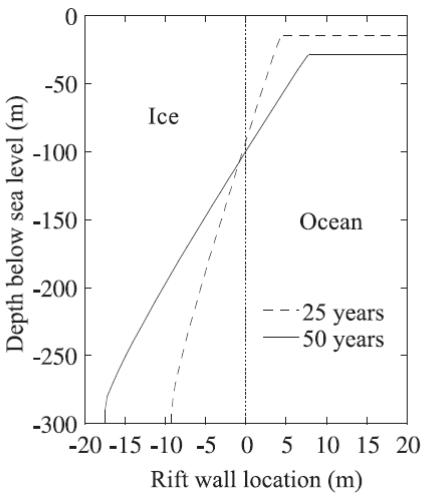

Figure 1.7: The profile of the rifts wall after a 25-year integration and at the end of a 50-year standard experiment compared with the initial wall location (which is represented by the vertical dotted line at the middle of the horizontal axis). The horizontal extensions of the two curves at the top indicate the interface between the accumulated ice and the water at the corresponding times. Over time the ice-ocean interface changes from vertical to sloping, driven by melting lower down in the water column and freezing higher up. Notice that the horizontal distance scale is exaggerated relative to the vertical one. Figure sourced from *Khazendar and Jenkins* (2003)

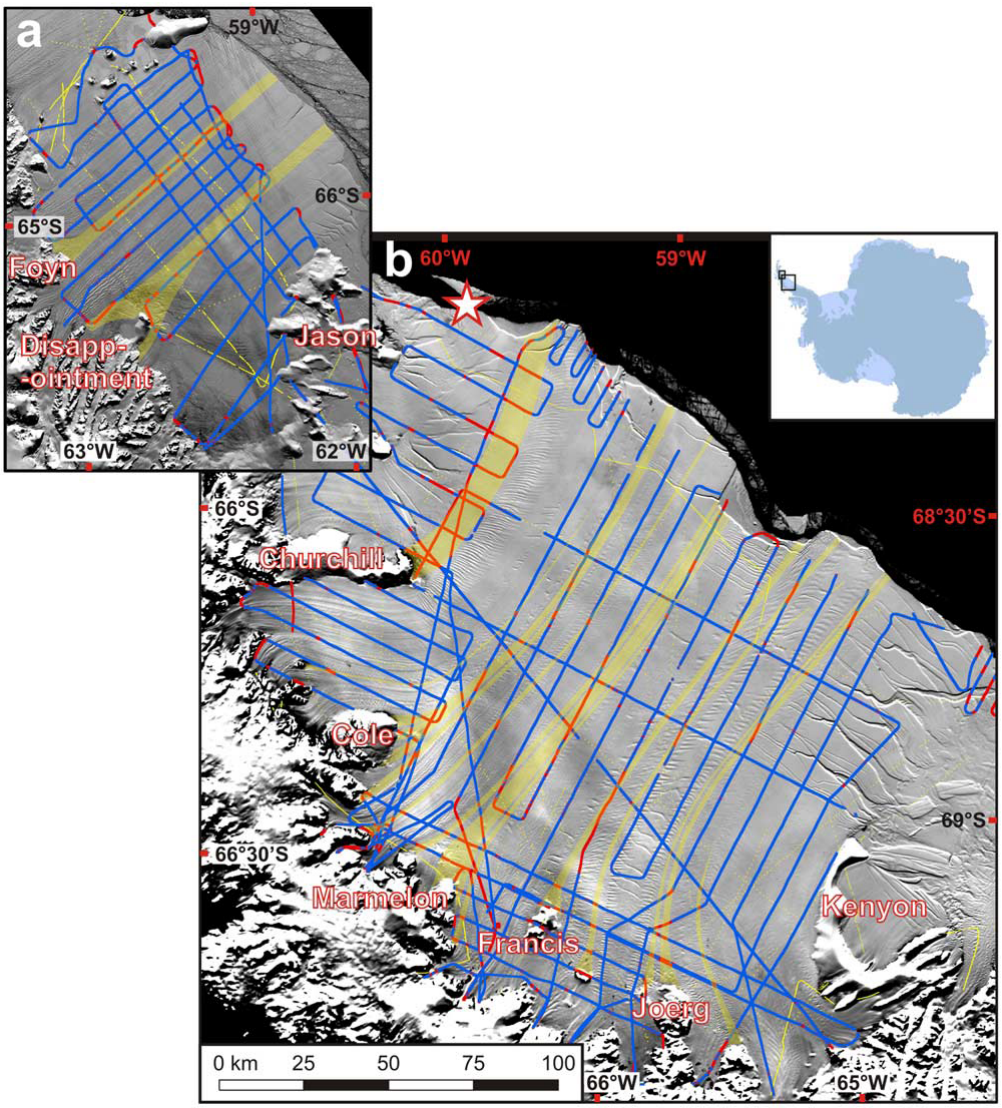

Figure 1.8: (a) 1986 Landsat image of LBIS (*Sievers et al.*, 1989) and (b) 2003–2004 MOA image of LCIS *Scambos et al.* (2007), both with 97–98 survey data. Red and (overlain) blue points mark surface and basal returns, so visible red points indicate failure to detect the base. Yellow shading indicates proposed marine ice and yellow tracks are other surveys incorporated in the ice draft. Figure sourced from *Holland et al.* (2009)

1.6 Conditional instability of frazil ice

Frazil-laden water, such as an ISW plume, can be considered a two-component mixture of ice and seawater (*Jenkins and Bombosch*, 1995; *Khazendar and Jenkins*, 2003; *Holland and Feltham*, 2005). It has been suggested that the presence of frazil ice can lead to a conditional instability in seawater (*Foldvik and Kvinge*, 1974), which proceeds as follows. Any frazil forming in the water column reduces the bulk density of a parcel of frazil-seawater mixture, causing it to rise. This rising causes the parcel to become further supercooled due to the increase in the freezing point with decreasing pressure. This causes more frazil to form, causing the parcel to accelerate, and so on. *Foldvik and Kvinge* (1974) analysed this instability by considering the change in temperature of a parcel of water rising through a variety of fixed water columns, arguing that the release of cool, salty water by this convection process may reach the seabed and contribute to the formation of AABW. Although the parcel of frazil-seawater mixture is less dense than the surrounding water, this is solely down to the frazil ice. Once the frazil ice leaves the parcel, for example by depositing onto the underside of sea ice, the remaining water is denser than the surrounding water due to an increased salinity from brine rejection. It is this remaining water that contributes to AABW formation. This process is summarized in schematic form in Fig. 1.9.

For this instability to occur, there must be net ice growth as the frazil-seawater parcel rises. The frazil growth rate is determined by the thermal driving, the difference between the temperature of the seawater in the parcel and the local freezing temperature. The instability can only occur if there is a tendency for the thermal driving to decrease (become more negative) as the parcel rises. If, for example, the parcel rises into sufficiently warmer waters, the frazil could melt and the instability would then be terminated. If, on the other hand, the water column is such that the decrease

in thermal driving due to pressure release is not overcome, the instability exists. Waters that get colder towards the surface are the norm in the salinity-stratified Southern Ocean.

However, this instability is not purely a function of the ambient water temperature. The rate of supercooling due to pressure release depends upon the rate at which the parcel rises, which is determined by its buoyancy. The relative buoyancy of the parcel as it rises is determined by the density and stratification of the water column. The buoyancy is also determined by the volume of frazil in the parcel. The rate of change of buoyancy of the parcel (i.e. the tendency of perturbations to grow) is therefore determined by the frazil growth rate per unit supercooling, which is a function of the detailed geometry of the frazil ice (i.e. its surface area per unit volume). Furthermore, any tendency of the parcel to mix due to turbulence as it rises will weaken its buoyancy and thermal contrasts and thus weaken the instability. Finally, buoyant frazil ice has a tendency to rise relative to its surrounding fluid, raising the possibility that such relative motion will negate the instability by removing the buoyancy forcing from the parcel of seawater containing the supercooling. Frazil ice may also leave the parcel through deposition onto an ice shelf base, removing the buoyancy forcing. This rate of deposition is affected by the ice shelf plume speed.

These considerations suggest that the frazil ice instability is far more complex than the original suggestions of *Foldvik and Kvinge* (1974). In particular, the viability and growth rate of the instability is expected to be governed by the rate of change of water temperature with height, the buoyancy of the perturbation, the density stratification, the details of the frazil crystal geometry, the level of turbulent mixing, and the rising of frazil relative to the surrounding seawater. No modelling study of this phenomenon has been carried out, and investigating under what conditions the instability is likely to exist and the factors that effect its strength may help to better understand ice formation in the Antarctic and hence the production of

AABW. There have been no previous modelling studies of the conditional instability of frazil ice. *Hughes et al.* (2014) use a 1 dimensional plume model to study the effects of frazil ice on an ISW plume, and find that the presence of frazil ice in an ISW plume can enhance its extent, leading to the supercooled water being present further from the ice front.

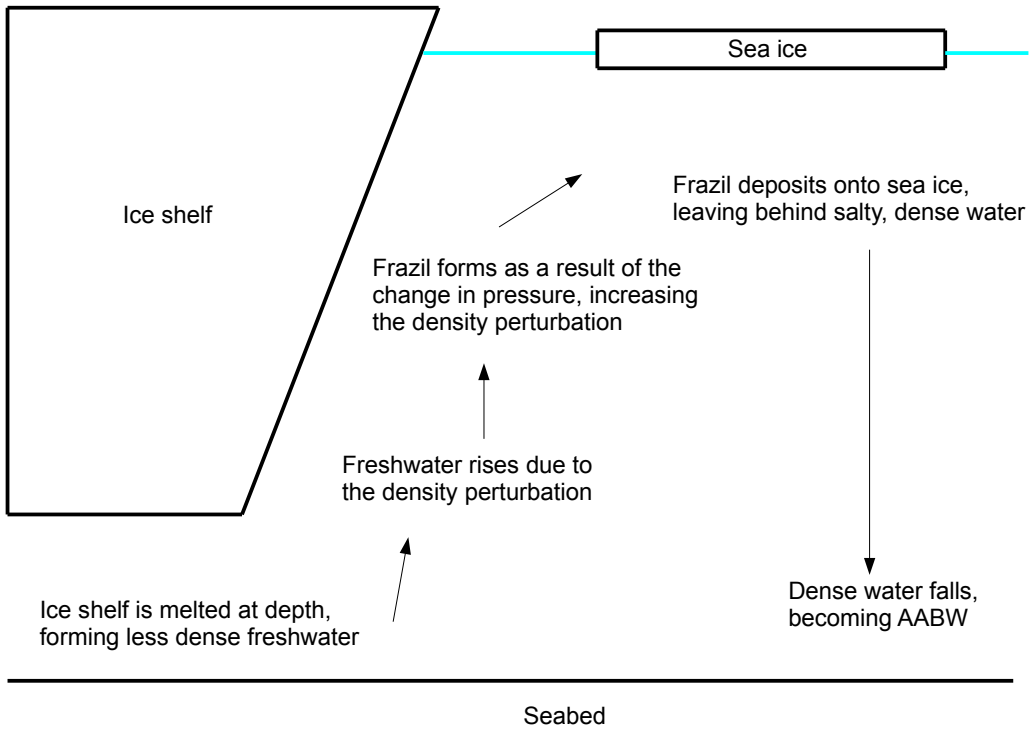

Figure 1.9: Schematic of frazil ice instability in an ISW plume.

1.7 Overview of the Thesis

This thesis aims to better understand these two particular areas of ice-ocean interaction, which as yet have been little studied. Chapter 2 provides an overview of Fluidity, the ocean-ice model used throughout this work. The full Navier-Stokes equations are described as well as the frazil ice model of *Jenkins and Bombosch* (1995) and its implementation into Fluidity. The results of validating the frazil ice model are then presented.

Chapter 3 uses this model to investigate ice ocean interaction in ice shelf basal crevasses, and its implications for ice shelf instability. The majority of the work presented in this chapter was published in *Journal of Geophysical Research: Oceans* in February 2014 (*Jordan et al.*, 2014). The setup for a model of an idealised crevasse is discussed, and this model is then tested and validated against the observations of *Orheim et al.* (1990). A sensitivity study into how various features affect the freeze rate and oceanic flow within the crevasse is then undertaken using the validated model as a baseline case. Model results show two different flow régimes, one dominated by freezing and one dominated by melting. Frazil ice is found to be responsible for the vast majority of all freezing in crevasses, and it is shown that under the right conditions freezing within basal crevasses could act as a stabilising influence on ice shelves. Finally, the model is used to investigate whether ocean melting can be solely responsible for the observed widening of basal crevasses as they approach the calving front. Oceanic forcing is found to be unable to be solely responsible for the widening of basal crevasses.

Chapter 4 uses the model to investigate the conditional instability of frazil ice growth in seawater. As of the time of writing the majority of the work presented in this chapter has been submitted for publication in *Journal of Physical Oceanography* and received a decision of minor corrections. Any frazil forming in the water column

reduces the bulk density of a parcel of frazil-seawater mixture, causing it to rise. Due to the pressure-decrease in the freezing point, this causes more frazil to form, causing the parcel to accelerate, and so on. The model set up to investigate this instability is presented, and the conditions investigated under which such an instability can exist. A sensitivity study into the factors effecting its existence is then carried out, and model results show that the amount of thermal driving, density gradient, background mixing and the size of an initial perturbation can each prevent the formation of the instability. Next, the set up for a second model representing the area in the vicinity of an ice front is discussed. Model results show that the instability can be responsible for significant amounts of ice growth up to several kilometres from an ice front, which could have implications for the formation of AABW.

Finally, Chapter 5 discusses and summarizes the conclusion that can be drawn from the previous two chapters. Future applications of the model and and potential new areas for research are also discussed.

2 Model and governing equations

This chapter beings with an introduction to Fluidity and its governing equations. The frazil ice model of *Jenkins and Bombosch* (1995) is then described, as well as the implementation of this model within Fluidity together with its validation. Finally, the ice shelf melting model implemented into Fluidity by *Kimura et al.* (2013) is discussed.

Fluidity is an open source, general purpose, multi-phase CFD (Computational Fluid Dynamics) code capable of solving numerically the Navier-Stokes and accompanying field equations on arbitrary unstructured finite element meshes in one, two and three dimensions. As such it is very well suited for the small scale processes and complex geometries involved in ice-ocean interactions in and around ice shelves.

2.1 Governing Equations

Fluidity assumes that the density of the fluid is represented by a two-component mixture of seawater, which is a linear function of temperature T and salinity S, and ice (*Jenkins and Bombosch*, 1995). This gives us a density equation of:

$$\rho = \rho_0(1 - C)[1 + \beta(S - S_0) - \alpha(T - T_0)] + \rho_i C, \tag{2.1}$$

where ρ is the density of the ice-seawater mixture, $\rho_0 = 1030$ kg m^{-3} is the reference density of seawater, $\alpha = 3.87 \times 10^{-5}$ °C^{-1} is the thermal expansion coefficient, T is the temperature, $T_0 = -2$ °C is the reference temperature, $\beta = 7.86 \times 10^{-4}$ psu^{-1} is the haline contraction coefficient, S is the salinity, $S_0 = 34.5$ psu is the reference salinity, $\rho_i = 920$ kg m^{-3} is the ice density and C is the dimensionless frazil ice concentration (volume of ice per unit volume of ice-seawater mixture).

Under the Boussinesq assumption equations of state are cast in a non-rotating Cartesian coordinate system (x, y, z). The domain considered in all of this work is relatively small and the Rossby radius, the length scale at which rotational effects become important, is equal to $Lr = \frac{\sqrt{gD}}{f}$, where D is the depth of the water and f is the Coriolis parameter. Assuming an average ice shelf is at a latitude of 70^0 with $D = 400$ m then the Rossby radius is roughly 3500 km and so the effects of rotation can be safely ignored. The resulting field equations describing the temporal evolution of the instantaneous velocity field $\vec{\mathbf{u}}(x, y, z, t) = (u, v, w)$, T, S and C in accordance with *Holland and Feltham* (2005) are

$$\nabla \cdot \vec{\mathbf{u}} = 0, \tag{2.2}$$

$$\frac{D\vec{\mathbf{u}}}{Dt} = -\frac{1}{\rho_m}\nabla P - g\frac{\rho}{\rho_m}\hat{k} + K_\nu \nabla^2 \vec{\mathbf{u}}, \tag{2.3}$$

$$\frac{DT}{Dt} = K_T \nabla^2 T + \left(T_c - T - \frac{L}{c_p}\right) w_c, \tag{2.4}$$

$$\frac{DS}{Dt} = K_S \nabla^2 S - S w_c, \quad \text{and} \tag{2.5}$$

$$\frac{DC}{Dt} + w_i \frac{\partial C}{\partial z} = K_C \nabla^2 C - w_c, \tag{2.6}$$

where $\frac{D}{Dt} = \frac{\partial}{\partial t} + \mathbf{u} \cdot \nabla$ is the material derivative, $g = 9.81$ m s^{-2} is the acceleration due to gravity, $\rho_m = 1030$ kg m^{-3} is the characteristic mixture density, K_ν, K_T, K_S and K_C represent the effective diffusivities of momentum, heat, salt and frazil ice respectively, the variable T_c is the temperature of the ice-ocean interface at the edge of a frazil crystal, the variable P represents the pressure, w_c is the melt rate of frazil ice per unit volume of mixture, w_i is the rising velocity of frazil ice and $\hat{k}$ is the vertical unit vector. All quantities are subject to a uniform, isotropic turbulent diffusivity/viscosity of 10^{-3} m^2 s^{-1} unless otherwise stated. With typical velocities of the order of a few centimetres, this gives a Reynolds number of the order of 10^3 over the length scale of an ice shelf basal crevasse. Over the 10 m length scale of the model mesh, however, we are much better able to resolve this turbulence. The second term on the right hand sides of (2.4) and (2.5) accounts for the temperature and salinity changes in a fixed volume of the water fraction due to a frazil crystal phase change.

Fluidity uses triangular cells for it's finite element mesh. Velocities are defined on a discontinuous galerkin mesh, whilst pressure is defined on a continuous mesh. All other variables (temperature, salinity, frazil concentration, etc.) are defined on the pressure mesh and are spatially discretised using a control volume method.

Solid boundaries, such as an ice surface or a sea bed boundary, are simulated with no slip velocity boundary conditions and as such have no flow in the direction parallel to the boundary on the boundary (ie, $\mathbf{u} = 0$). Zero-flux conditions for heat, salt and frazil are applied at the seabed. Inflow boundary conditions in the model are steady Dirichlet boundary conditions, where temperature, salinity, velocity and frazil ice concentration are prescribed along the boundary. Outflow boundary condition are zero-flux Neumann boundary conditions. Preliminary work found that using strongly applied boundary conditions caused problems at the inflow boundary, causing anomalously high velocities. As a result all boundary conditions are now

'weakly' applied; conditions are not rigidly applied along a boundary but are allowed to relax.

Model meshes throughout this work have been generated using GMSH, a 3D finite element grid generator. The resolution in areas of interest, such as inside a basal crevasse, is set to be higher. Whilst Fluidity has the ability to adapt mesh resolution within the simulation this capability has not been used, as the areas of interest in this work remain in a static, fixed location.

2.2 Frazil ice model

Frazil ice can be modelled by either representing the distribution of ice crystal sizes (*Smedsrud and Jenkins*, 2004; *Holland and Feltham*, 2005; *Galton-Fenzi et al.*, 2012) or, more simply, by using a single representative size class (*Jenkins and Bombosch*, 1995). The use of multiple size classes requires several additional tracers, so for computational simplicity the single-size-class frazil ice model of *Jenkins and Bombosch* (1995) has been incorporated into Fluidity for this study. This is justified on the grounds that in both application areas we seek a basic qualitative study of the effect of frazil ice rather then exact quantitative answers. Sensitivity studies are undertaken to ascertain the effect of varying this single representative size class, in particular it is found that the changing the crystal radius has a large effect upon the growth rate of frazil ice, if not the total amount of ice grown.

2.2.1 Frazil ice dynamics

Fluidity already has a sediment model (*Parkinson et al.*, 2014) that has previously been used to develop a full multi-phase (both water and ice) model of fluid-particle mixtures to simulate volcanic ash settling into water (*Jacobs et al.*, 2012). In many

ways this is analogous to frazil crystals in water, only with frazil rising rather than sediment falling. This is done in Fluidity by setting the submerged specific gravity and sinking velocity to be negative, as the density of ice is less than seawater. This will have the effect of lowering the bulk density of seawater where frazil ice is present and also giving the frazil ice a rising velocity relative to the seawater containing it. Frazil ice has submerged specific gravity, R:

$$R = \frac{\rho_i - \rho_w}{\rho_w}, \tag{2.7}$$

where ρ_i is the density of ice and ρ_w the density of seawater. While calculating R it is assumed that $\rho_i = 920$ kg m^{-3} and $\rho_w = 1030$ kg m^{-3}, giving $R = -0.107$. The frazil rise velocity w_i relative to the moving fluid is approximated by frazil's buoyant drift velocity in still water (*Gosink and Osterkamp*, 1983):

$$w_i^2 = \frac{4Rgr\epsilon}{C_d}, \tag{2.8}$$

where r is the chosen radius of frazil ice discs, $g = 9.81$ m s^{-2} is the acceleration due to gravity and $\epsilon = 1/16$ is the aspect ratio of the frazil ice disc (*Clark and Doering*, 2006). Laboratory experiments find that the distribution of frazil crystal radii takes a log normal form, with mean radii ranging from 0.35 mm to 1 mm (*Ye et al.*, 2004; *Clark and Doering*, 2006; *McFarlane et al.*, 2014), whilst field observations have measured crystal radii of the order of 1 cm (*Dieckmann et al.*, 1986; *Robinson et al.*, 2010). The mean distribution by volume is skewed towards smaller crystal radii and so it was decided to focus on these smaller crystal radii for this work. As a result it is assumed r=0.75 mm for the baseline representative frazil crystal radius. Sensitivity studies will be carried out to ascertain the effect of varying the frazil crystal radius. The drag coefficient C_d varies considerably with the disc Reynolds number, defined

as:

$$Re = \frac{w_i 2r}{\nu}, \tag{2.9}$$

where $\nu = 1.95 \times 10^{-6}\text{m}^2\ \text{s}^{-1}$ is the kinematic viscosity of seawater. *Gosink and Osterkamp* (1983) used published experimental data on the drag coefficient of discs of varying sizes to determine the following empirical relationship:

$$\log_{10}(C_d) = 1.386 - 0.892 \log_{10}(Re) + 0.111(\log_{10}(Re))^2. \tag{2.10}$$

By using an iterative method an estimate for w_i for a given crystal radius can be calculated from (2.8), (2.9) and (2.10).

When frazil ice comes into contact with an ice boundary it is assumed to freeze onto the boundary and leave the fluid. The total flux through an ice boundary, and hence the frazil ice deposition rate, is calculated via:

$$\frac{\partial \eta}{\partial t} = nikiw_b C_b, \tag{2.11}$$

where η is the thickness of frazil ice in metres, C_b is the volumetric frazil concentration at the ice shelf ocean boundary and w_b is the component of w_i normal to the boundary (adapted from *Parkinson et al.* (2014)). Resuspension of frazil ice crystals has been ignored in this work, as it is assumed that the crystals will adhere to the ice boundary. w_b is orientated directly upwards, so frazil cannot deposit onto vertical walls. The particular model set ups described in the following chapters use 'weakly applied' no-slip velocity boundary conditions. As a result of this some flow normal to the ice-ocean boundaries is present as an artefact of the numerical solution. This creates a negligible amount of frazil ice deposition onto any vertical walls, which has been ignored in any calculation of freeze rate. The rate of frazil deposition is combined with direct freezing (*Kimura et al.*, 2013) to give a total freeze rate for an

ice-ocean boundary. In this work melting is defined as negative freezing.

2.2.2 Frazil ice thermodynamics

The growth of frazil ice acts as a source of heat and salt in the temperature and salinity equations due to the release of latent heat and brine rejection (*Jenkins and Bombosch*, 1995). The ice-ocean interface at the edge of a frazil crystal is assumed to be at the freezing temperature, so the temperature and salinity are related by a linear expression for the pressure freezing point of seawater:

$$T_c = aS_c + b + cz_c, \tag{2.12}$$

where T_c and S_c are the temperature and salinity at the edge of the frazil ice crystal, the variable z_c represents the elevation and a, b and c are the constants -0.0573 °C PSU $^{-1}$, 0.0832 °C and 7.61×10^{-4} °C m^{-1} respectively. Balancing heat and salt transfer through the frazil boundary layer with the latent heat and freshwater release of melting obtains:

$$(1-C)\gamma_T^c(T-T_c)\frac{2C}{r} = \frac{L}{c_0}w_c, \tag{2.13}$$

$$(1-C)\gamma_S^c(S-S_c)\frac{2C}{r} = w_c S_c, \tag{2.14}$$

where $L = 3.35 \times 10^5$J kg^{-1} is the latent heat of ice fusion, $c_0 = 3974$ J kg^{-1} °C^{-1} is the specific heat capacity of sea water, w' (s^{-1}) is the melt rate of frazil ice volume per unit volume of mixture, and γ_T^c and γ_S^c are the ocean heat and salt transfer coefficients at the edge of frazil ice crystals. For transfer at the disc edges the appropriate length scale is the half-thickness of the disc (*Daly*, 1984), so the

transfer coefficients are calculated as follows:

$$\gamma_T^c = \frac{\mathrm{Nu}\kappa_\mathrm{T}}{\epsilon r}, \gamma_S^c = \frac{\mathrm{Nu}\kappa_\mathrm{S}}{\epsilon r} \tag{2.15}$$

where $\kappa_T = 1.4 \times 10^{-7}$ m^{2}s^{-1} is the molecular thermal diffusivity of seawater, $\kappa_S = 8 \times 10^{-10}$ m^2 s^{-1} the molecular haline diffusivity of seawater and Nu is the dimensionless Nusselt number, the ratio between convective and conductive heat transfer, which is assumed to be Nu=1. In reality the relative difference in salinity between the ice and seawater will cause the Nusselt number to vary, for simplicity, however, it is assumed to be 1.

This gives three equations and three unknown variables T_c, S_c and w'. To eliminate w' (2.13) is substituted into (2.14):

$$\gamma_T^c(T - T_c)\frac{c_0}{L} = \frac{\gamma_S^c(S - S_c)}{S_c} \tag{2.16}$$

Then T_c is eliminated by substituting (2.12) into (2.16):

$$\gamma_T^c(T - aS_c + b + cz_c)\frac{c_0}{L} = \frac{\gamma_S^c(S - S_c)}{S_c} \tag{2.17}$$

This can be rearranged into a quadratic in terms of S_c:

$$aS_c^2 - \left((T + b + c_z) + \frac{\gamma_S^c L}{c_0\gamma_T}\right) S_c + \frac{S\gamma_S^c L}{c_0\gamma_T} = 0 \tag{2.18}$$

There are two solutions to (2.18), one positive and one negative. As salinity can by definition never be negative the value of S_c is deemed to be the positive solution to (2.18). This can then be used to eliminate S_c from (2.14) and thus solve for w'. As these equations require some frazil to be present before any freezing can occur, a very small minimum concentration of frazil ($C_{\mathrm{min}} = 5 \times 10^{-9}$) is used when

$C < C_{\min}$ in the solution of (2.16)–(2.18). This background concentration is only used to determine frazil growth rates and is not part of the frazil ice concentration conserved in the model, as in *Jenkins and Bombosch* (1995).

The formation of frazil ice provides a source of heat and salt, the full derivation of which is shown in *Holland and Feltham* (2005):

$$\frac{DT}{Dt} = w_c \left(\frac{L}{c_0} + T - T_c \right) \tag{2.19}$$

$$\frac{DS}{Dt} = w_c S \tag{2.20}$$

where δT and δS are the change in temperature and salinity per second due to the growth of frazil ice. When frazil is formed or melted these two equations provide a source or sink term within the model domain for heat and salt respectively.

2.2.3 Implementation of frazil ice model in fluidity

As previously stated, the frazil ice model of *Jenkins and Bombosch* (1995) has been implemented in Fluidity. This has been done by modifying a sediment field to represent frazil ice crystals rather than sediment particles. At each point of the model mesh the concentration of frazil ice is defined, and this concentration affects the bulk density of the fluid at this point (2.1). In addition to the frazil crystals rising velocity relative to the fluid they are subjected to a uniform isotropic diffusion. At each time step w' is calculated for each mesh point, applied constantly between each time step. It is also assumed that, as w' is defined in terms of melting, negative values of w' cause freezing. The constant rate of w' used causes no problems in the freezing case, however problems can arise during a melting case if the melt rate applied at one time step would cause there to be negative frazil ice concentration at

the next. To prevent this the value of w' used in such cases is set to be such that at the end of the time step the frazil concentration will be exactly 0. This revised value of w' is then used for the temperature and salinity changes caused by frazil ice.

2.2.4 Validation of frazil model

The implementation of the frazil ice model has been validated against calculations of latent heat change by cooling a 1 m two dimensional square of water at sea level by a given amount. The temperature, salinity and frazil ice concentration change in the model are then compared to expected values. As the model assumes a single representative size class, the effects of varying the frazil crystal radius is also shown. In the validation test the water is cooled to 0.1°C below the freezing point. The model will always form frazil ice provided there is supercooled water, and in the steady state of the model it is expected that enough frazil will have formed to eliminate the thermal driving (Fig. 2.1a). There is a corresponding rise in temperature due to the latent heat of ice formation (Fig. 2.1b), although the total temperature change is slightly less than 0.1°C because of the increased salinity due to brine rejection lowering the freezing temperature (Fig. 2.1c). Finally, a final frazil ice concentration of 1.1863 $\times 10^{-3}$ is observed (Fig. 2.1d). If seawater is cooled by imposing a negative thermal driving ($T^* < 0$) below the freezing point the total change in frazil ice concentration is given by:

$$\int \frac{dC}{dt} dt = \frac{-T^* C_0}{L} \tag{2.21}$$

The model results do indeed match this value. Varying the crystal radius has no effect on the temperature, salinity or frazil ice concentration changes, however it does effect the rate at which these changes occur. A small crystal radius has a greater

surface area to volume ratio than a larger crystal, and so freezes at a faster rate. The reverse for larger crystals is also true. Frazil crystal growth is non-linear, with the rate of growth being proportional to both the amount of thermal driving and the frazil ice concentration. This results in the fastest growth of frazil ice being seen during the middle of the simulation, where there is both a large amount of thermal driving remaining and some initial frazil crystal formation has already taken place.

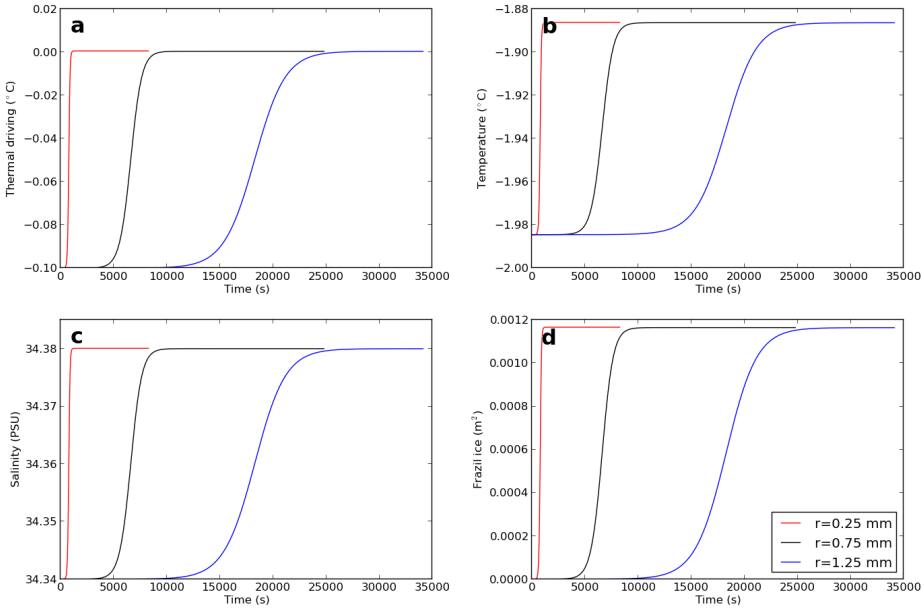

Figure 2.1: Validation of frazil ice model. Modelled change in (a) thermal driving, (b) temperature, (c) salinity and (d) amount of frazil ice in a 1 m^2 box of water at sea level cooled by 0.1 °C is shown for r=0.25 mm (blue), r=0.75 mm (black) and r=1.25 mm (red).

2.3 Ice shelf melt model

Direct melting and freezing onto ice shelves has been implemented in Fluidity by *Kimura et al.* (2013). This has been achieved by applying thermodynamic boundary conditions at the ice-ocean interface. The temperature at the ice-ocean interface (T_b) is at the local freezing temperature, determined by the salinity at the ice-ocean interface (S_b) in a similar fashion to (2.12):

$$T_b = aS_b + b + cz_b \tag{2.22}$$

where z_b is the elevation of the ice-ocean interface relative to sea level. The local freezing relation is linked with the balance of heat and salt fluxes between the ice and ocean (*Jenkins and Bombosch*, 1995; *McPhee*, 2008):

$$m'L + m'c_0(T_b - T_\infty) = c_0\gamma_T u_\infty(T_\infty - T_b) \tag{2.23}$$

$$m'S_b = \gamma_S u_\infty(S_\infty - S_b) \tag{2.24}$$

where $c_I = 2009$ J kg^{-1} °C^{-1} is the specific heat capacity of ice, m' the melting freshwater flux velocity of the ocean in the direction normal to the ice-ocean interface, $T_I = -25$ ° C the far-field internal temperature of ice, T_∞ the far field ocean temperature, S_∞ the far field ocean salinity and u_∞ the speed of ocean flow oriented parallel to the ice shelf in the far field, which is taken to be the source of turbulence that drives the mixing of heat and salt towards the ice. The melt rate of ice is defined as $m = \frac{m'\rho_w}{\rho_i}$. The resulting heat ($F_H$) and salt ($S_H$) fluxes to the ocean are calculated according to *Jenkins et al.* (2001).

$$F_H = c_0(\gamma_T u_\infty + m)(T_\infty - T_b) \tag{2.25}$$

$$F_S = (\gamma_S u_\infty + m)(S_\infty - S_b) \tag{2.26}$$

The three unknowns, T_b, S_b, and m, are solved by combining (2.22)–(2.3) to produce a quadratic equation. Similarly to (2.18), one solution of S_b is positive definite. This approach is applied to calculate a melt rate on any element boundary surface that is defined to be ice. A negative melt rate in this case represents direct freezing.

3 Modelling ice-ocean interaction in idealised ice shelf basal crevasses

3.1 Overview

This chapter shows how the model described in Chapter 2 has been used to study ice-ocean interactions and ocean dynamics in ice shelf basal crevasses. The particular model set-up of the model described in Chapter 2 is described, and then validated by a comparison with observational data. A sensitivity study is then undertaken around this validated baseline case. As the model is validated against a rectangular crevasse the effect of varying the geometry to represent a triangular crevasse is then discussed. Finally, work looking at whether the ocean can be solely responsible for the observed widening of crevasses as they propagate towards the calving front is presented. Most of the work in this chapter has been published in *Journal of Geophysical Research: Oceans* as *Jordan et al.* (2014).

3.2 Model set-up

As there is no observational data of oceanic conditions inside an ice shelf basal crevasse it has been decided to calibrate the model against the only set of comparable data available, namely the observations of the Jutulgryta rift made by *Orheim et al.* (1990). A rift differs from a crevasse in that it extends through the entire ice shelf thickness unlike a crevasse which only extends part of the way, whether from the surface or the base. In the case of the Jutulgryta rift, however, a mélange of ice roughly 40 m thick had formed in the top of the rift, effectively 'capping' it and making it resemble a crevasse.

The model domain has been chosen to represent the dimensions of the Jutulgryta rift. The domain is a two-dimensional rectangular channel 5 km long in the streamwise (x) and 100 m in the vertical (z) directions, representing a section of the cavity beneath an ice shelf (Fig. 3.1). The upper surface is considered glacial ice and the bottom seabed. A single, idealised rectangular basal crevasse 260 m wide by 340 m deep is placed in the middle of the ice shelf, making the water column thickness 440 m at its thickest. By using a finite-element ocean model the grid resolution can be increased in areas of interest while maintaining a coarser resolution elsewhere, reducing the computational expense. As such, mesh resolution is 20 m except in the crevasse, where a higher resolution of 5 m has been used. A timestep of 5 s was used in all simulations in order to obtain a Courant number < 1. An inflow enters the domain from the upstream side (left, x=0) under steady Dirichlet boundary conditions ($w = 0$, $u = U_{in}$, $T = T_{in}$, $S = S_{in}$ and $C = 0$) and leaves via the downstream side (right, x=5 km) with zero-flux Neumann boundary conditions ($\frac{\partial u}{\partial x} = \frac{\partial w}{\partial x} = \frac{\partial T}{\partial x} = \frac{\partial S}{\partial x} = \frac{\partial C}{\partial x} = 0$). No-slip boundary conditions are weakly applied in discretised space (allowing the existence of a boundary layer) at the ice shelf boundary and the seabed. Zero-flux conditions for heat, salt and frazil are applied

at the seabed.

3.2.1 Model calibration

The model has been calibrated to reproduce the observed temperature and salinity profiles and freezing rate within the Jutulgryta rift. Reproducing the observed 60 m of supercooling and $\sim$ 1 m yr^{-1} freezing rate observed by *Orheim et al.* (1990) was given priority, as conditions within the rift are of more interest to this study than conditions outside the rift. In keeping with these observations, a constant initial temperature and salinity of -1.965 ° C and 34.34 psu has been used, with a constant 0.025 m s^{-1} inflow velocity with the same temperature and salinity as the initial conditions. This water mass crosses the freezing temperature at 60 m from the the top of the crevasse. A frazil crystal radii of 0.75 mm has been used as the single representative size class for the frazil ice model described in Chapter 2.

When compared with observations (Fig. 3.2) it is possible to obtain a matching 'calibration' temperature profile within the rift, including the 60 m of supercooled water at the top. The salinity profile is a good fit over the majority of the crevasse, except for the failure to reproduce the slight freshening observed at the top of the crevasse. This could be a result of the model imposing a distinct boundary at the ice-ocean interface at the top of the crevasse, whereas in reality there is a continuum between ocean, ice and a mixture of the two. The model cannot reproduce the conditions observed outside the rift, below about 300 m, which are governed by the general circulation in the Fimbulsen cavity (*Hattermann et al.*, 2012). The ocean modelled freezing rate was found to be 1.2 m yr^{-1} at the top of this profile, which compares favourably with the observed ice growth rate of 2 m after 2 years in their single profile. However, as shown by the results below, salinity and temperature within the modelled rift are not horizontally uniform, and so there will always be

a considerable uncertainty in the calibration. Fig. 3.2 also shows a 'comparison' profile from near the upstream boundary in the rift, and it is clear that in this location the supercooling has been taken up to a greater extent by frazil ice growth. At the top of this profile there is a correspondingly larger freezing (of 16 m yr^{-1}). Since there are only observational measurements at a single location within the rift, the strongest calibration it is possible to perform is to match the behaviour of one location in the model. The evolution over time of maximum frazil ice production, maximum supercooling, maximum velocity magnitude and maximum ice shelf melt rate are shown in Fig. 3.3. It is immediately apparent that freezing within a crevasse creates an inherently complex, chaotic system in this model. Due to the lack of any observable long term trends after the initial few days of model run time it has been assumed that averaging results over the two week period following day 10 will provide representative results of the system. This calibrated set-up has been used as a baseline case for a variety of sensitivity studies.

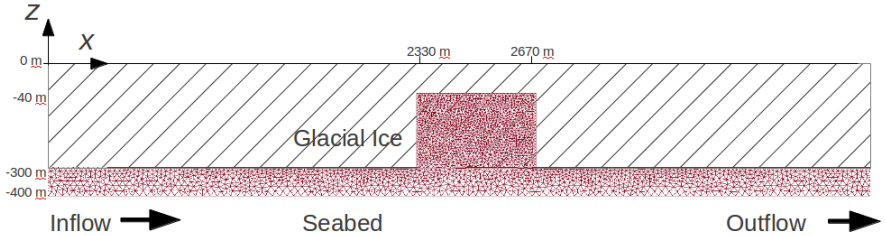

Figure 3.1: Model mesh. Resolution varies from 5 m inside the basal crevasse to 20 m outside. A flow past the crevasse is imposed from left to right.

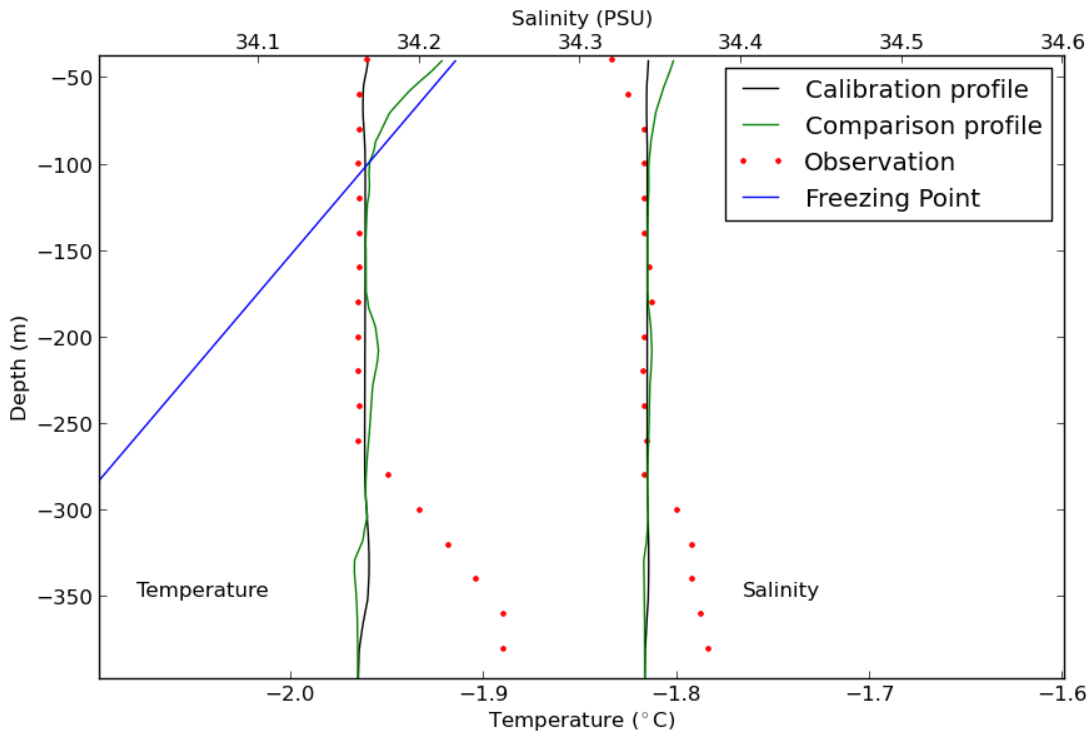

Figure 3.2: Model calibration. The modelled calibration profiles of salinity and temperature are shown in black, with comparison profiles shown in green and observations shown in red (*Orheim et al.*, 1990; *Khazendar and Jenkins*, 2003). The freezing point of the inflow water is shown in blue.

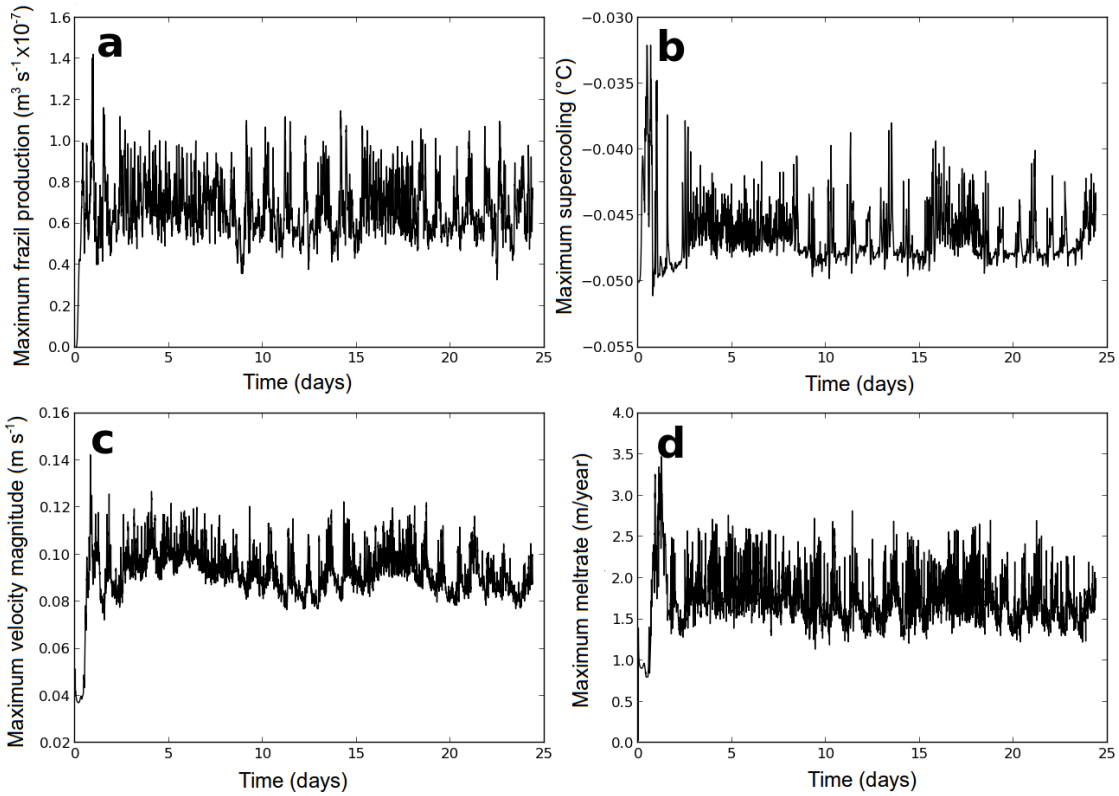

Figure 3.3: (a) Maximum frazil ice production, (b) maximum supercooling, (c) maximum velocity magnitude in the crevasse and (d) maximum ice shelf melt rate for the baseline/calibration case.

3.3 Base case

To provide a general overview, Fig. 3.4 shows the density in the base case and a schematic illustration of the oceanic flow field. Flow enters from the left and is sufficiently warm to melt the base of the ice shelf outside the crevasse. Melting of the ice shelf provides a source of relatively cool and fresh meltwater which is less dense than the surrounding water. The meltwater rises up into the basal crevasse on its downstream side until, roughly 60 m from the top by construction, it reaches its freezing point and becomes supercooled. This supercooling leads to frazil ice formation within the water column, but not quickly enough to remove all the supercooling, so the supercooled water continues rising to the top of the crevasse, aided by the buoyancy of the frazil ice. Direct freezing occurs on the top and upper sides of the crevasse. Freezing, both direct and through frazil ice production, creates relatively warmer and saltier water by the release of latent heat and freshwater extraction. Some frazil ice accretes to the ice shelf base, so the water left behind is denser than the water below it, creating an overturning circulation within the entire crevasse that is inherently statically unstable. The dense water descends down the upstream side of the crevasse and is then partially vented into the passing flow.

A closer inspection of the model results (Fig. 3.5) shows that the time-averaged velocity of the circulation is greater than the inflow velocity, leading to greater rates of melting and freezing within the crevasse than outside it. The passing flow beneath the crevasse forces the overturning circulation to move in an anticlockwise direction (Fig. 3.5a), with colder meltwater rising up on the downstream side, freezing at the top and then returning warmer on the upstream side (Fig. 3.5a,b). Fig. 3.5b shows contours of thermal driving $T^* = T - (aS + b + cz)$, which represent the local potential to freeze or melt ice (where the quantity in parenthesis is the local freezing temperature). The thermal driving field leads to maximum frazil ice formation

on the upstream side of the supercooled upper region (Fig. 3.5c), as the frazil crystals multiply in the horizontal flow across the crevasse (Fig. 3.5a).This causes a significant lateral variation in the rate of ice deposition at the top of the crevasse, which accounts for the variation in model calibration results (Fig. 3.2). This can be seen in Fig. 3.5d, which shows the effect the calculated melt/freeze rate would have on crevasse geometry if maintained for 5 years (geometry changes not included in model). This freezing is dominated by frazil ice, as shown in Table 3.1. Ice is also directly melted on the lower half of the crevasse sides, and re-frozen higher up on the sides and at the top. This secondary effect would create a widening at the base of the crevasse and narrowing at the top, as predicted by *Khazendar and Jenkins* (2003), however the slight widening of the crevasse by direct melting is much less than the amount of frazil ice deposition at the top of the crevasse.

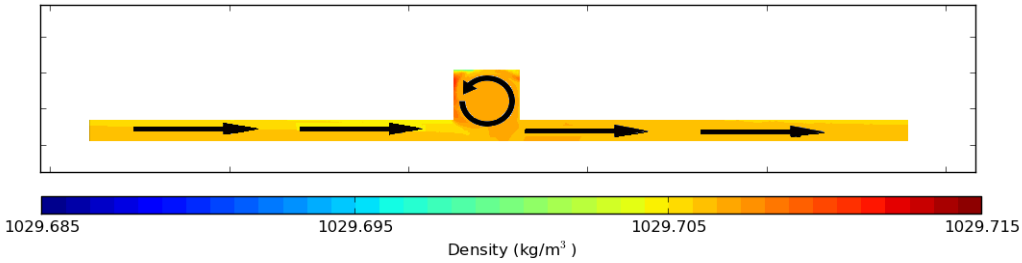

Figure 3.4: Overview of ocean dynamics for the whole domain in the baseline case. Flow enters from the left and leaves via the right. Meltwater rises into the crevasse and freezes on the top, creating a cold and saline dense layer. This dense layer enhances the overturning circulation within the crevasse.

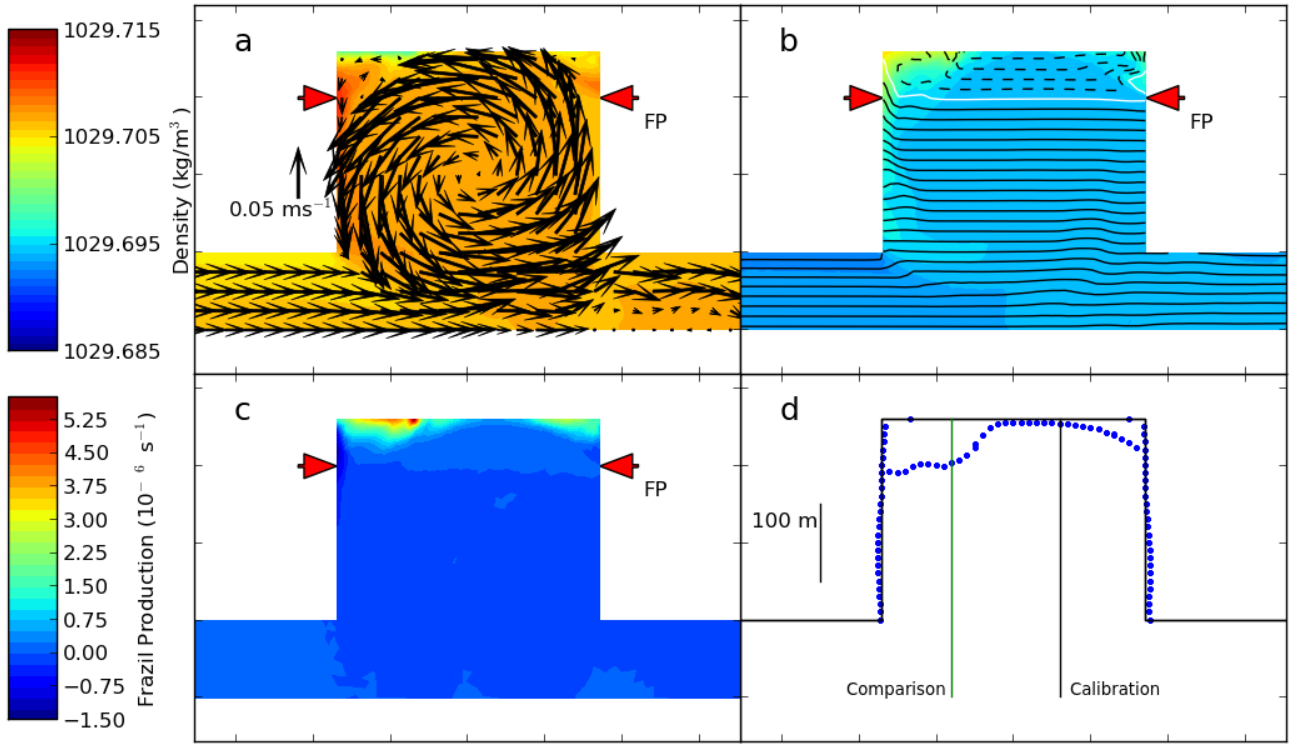

Figure 3.5: Baseline case showing (a) time-averaged mean density with mean velocity vectors, (b) mean temperature (colours) with mean thermal driving (contours), (c) mean frazil crystal production and (d) change in crevasse geometry as a result of mean melt rate maintained for 5 years with the position of the calibration and comparison profile shown in black and green respectively. The white contour in panel b is at zero thermal driving while black contours are every 0.1 degree above and black dashed contours are every 0.01 degree below this point. The pressure dependent freezing point (FP) of the water properties used for initial and inflow conditions is also shown.

3.4 Sensitivity study

To gain a qualitative understanding of ocean processes and melting and freezing in ice-shelf crevasses, the effects of varying ocean temperature, inflow velocity, crystal radius and crevasse geometry have been investigated in a set of sensitivity simulations. Specifically, these simulations have five different inflow and initial temperatures (T1 = -1.89 ° C, T2 = -1.93 ° C, T3 = -1.965 ° C (baseline), T4 = -1.99 ° C and T5 = -2.02 ° C), five different inflow velocities (U01 = 0.01 m s^{-1}, U025 = 0.025 m s^{-1} (baseline), U05 = 0.05 m s^{-1}, U10 = 0.1 m s^{-1} and U20= 0.20 m s^{-1}), seven different mean crystal radii (R025 = 0.25 mm, R065 = 0.65 mm, R070 = 0.7 mm, R075 = 0.75 mm (baseline), R080 = 0.8 mm, R085 = 0.85 mm and R150 = 1.5 mm), and five different crevasse geometries (260 m by 340 m (baseline), 260 m by 170 m, 130 m by 340 m, 260 m by 130 m crevasse with the cavity beneath the crevasse extended to 200 m and a triangular crevasse 340 m at the base and 240 m in height). Simulations without the frazil ice and/or direct melting and freezing were also performed. The pressure-decrease in the freezing temperature means that supercooling increases with height above seabed, so the temperature sensitivities were chosen to place the initial freezing point 20 m above the crevasse top (T1, i.e. no supercooling), 20 m below the crevasse top (T2), 60 m below the crevasse top (T3, baseline), 100 m below the crevasse top (T4) and 140 m below the crevasse top (T5) respectively. All settings except the one under investigation are held constant at their baseline values.

3.4.1 Temperature variation

In cases warmer than the baseline (Fig. 3.6a,b), there is less or no frazil and dense water production, so the circulation in the crevasse is primarily driven by meltwater as opposed to rejected brine. This leads to the buoyant meltwater rising up into the

Table 3.1: Average freezing rate and frazil ice contribution to freezing rate for the baseline, T2 (warmer than baseline), T3 (colder than baseline), R025 (smaller radii than baseline, R150 (larger radii than baseline). Freezing rates are spatially averaged over the top of the crevasse.

Run	Average freezing rate (m/a)	Frazil ice percentage contribution
Baseline	8.32	97.8
T2 (warm)	0.05	1.7
T4 (cold)	31.8	99.7
F025 (small crystal radii)	5.81	99.9
F150 (large crystal radii)	0.06	3.3

crevasse on the upstream side before leaving on the downstream. A simulation colder than the baseline has a greater amount of frazil growth within the crevasse and less melting outside (Fig. 3.6d). This leads to a greater production of dense water at the top of the crevasse and a faster and less stable overturning circulation. When there is significant frazil ice production in the crevasse the density of the water-ice mixture at the very top of the crevasse falls overall, even though the density of the water fraction has increased due to the greater salinity. In freezing dominated cases, such as T3 and T4, frazil ice precipitation has a higher proportion of the freezing rate than direct freezing (Table 3.1).

Warmer cases (Fig. 3.7a, b) have flatter thermal driving contours than the baseline case (Fig. 3.7c). At these temperatures the circulation is driven by meltwater rather than dense rejected brine, and this can be seen by the presence of slightly cooler meltwater along the sides and top of the crevasse. In the colder case (Fig. 3.7d) the contours are sloped, with colder water rising up the downstream side of the crevasse. The warmer, dense water produced by freezing can be seen descending down the upstream side. Significant amounts of supercooled water are in contact with the ice high up the downstream side and at the top of the crevasse, leading to freezing there (Fig. 3.8a). In melt dominated cases, such as T2, a higher proportion of the freeze rate results from direct freezing than deposition of frazil ice (Table 3.1).

Table 3.2: The effect of far field temperature on freeze rate.

Far field temperature (° C)	Average freeze rate (m/yr)
-1.93	0.9
-1.96	6.7
-1.99	25.3
-2.02	47.2

The results of an ocean-temperature sensitivity study show a nonlinear relationship between the 'far-field' temperature and the overall freezing rate (Table 3.2). The freezing rate for the coldest cases is so large, several tens of metres per year, that any crevasse with this amount of supercooled water will quickly fill in with marine ice and thus limit the amount of supercooling present. As such it would be highly unlikely for a crevasse to have much more than the observed 60 m of supercooling. This could also explain the rapid initial decrease in crevasse depth as they propagate towards the calving front seen by *Luckman et al.* (2012), assuming that the thermal driving is roughly laterally uniform in space. This sensitivity to temperature change is highly asymmetric, with a very small cooling filling a crevasse with marine ice, but a reversal of that cooling would take decades to melt the marine ice.

3.4.2 Velocity variation

Greater inflow velocities were found to create a stronger overturning circulation within the crevasse, due to the increased meltwater supply from outside the crevasse and the shear of the flow past the crevasse bottom. While the freezing rate generally increases with velocity, the overall magnitude remains largely the same (Fig. 3.8b). As the freezing rate is dominated by frazil ice production rather than direct freezing the velocity-driven increase in direct freezing is weak. The circulation in the crevasse is buoyancy driven, and while increasing the inflow velocity does increase melting outside the crevasse, and therefore the buoyancy, this has little effect on the flow in

the crevasse.

3.4.3 Frazil crystal size variation

Even with no freezing or melting in the model at all there is still a circulation driven by the shear past the crevasse (Fig. 3.9a), although this circulation is an order of magnitude slower than the inflow velocity and is negligible when compared with the baseline case (Fig. 3.9d). When only direct melting and freezing are used (Fig. 3.9b) the crevasse hosts a large amount of supercooled water, as direct freezing is too slow to quench the supercooling (Fig. 3.10a). As only a small amount of freezing is occurring a similar melt-driven flow pattern as with warmer temperatures (Fig. 3.9b) is observed, with only a hint of the brine-driven recirculation.

When frazil melting and freezing is activated, varying the size of frazil crystals dramatically changes the rate at which supercooling is quenched in the crevasse, and hence the amount of dense water production. Smaller crystals freeze faster due to their larger surface area per unit volume. For extremely small crystals, this has the effect of removing virtually all supercooling from the water column (Fig. 3.10b, $r = 0.25$ mm). Crucially, however, the smaller crystals have a very low rising velocity, so they remain in suspension and lower the density of the mixture (Fig. 3.9c). Larger crystals form at a slower rate, and so more supercooling is present in the crevasse; thermal driving contours are flat, and resemble the no-frazil case (Fig. 3.10d, $r = 1.5$ mm). Brine production slows down and the circulation returns to the meltwater-driven flow seen in other cases with low freezing rates.

It is important to note that the frazil radii used in Figures 3.9 and 3.10 are at the extreme ends of the range of radii observed in laboratory experiments (*Ye et al.*, 2004; *Clark and Doering*, 2006; *McFarlane et al.*, 2014) and are shown for illustrative purposes only. The model requires a single representative crystal radius, and these

extreme values will never be representative of the entire frazil population. When the frazil crystal radius is varied by a smaller amount around the baseline value the general, asymmetric pattern of freezing remains the same, although with a flattening of the spatial distribution (Fig. 3.8c). With smaller radii frazil ice is produced quicker, increasing deposition on the downstream side, whilst the slower forming larger radii deposit less on the upstream side. Once again, the freezing rate in freeze-dominated cases (low to medium crystal radii) is dominated by frazil ice precipitation, whilst melt-driven cases (high crystal radii) are dominated by direct freezing (Table 3.1).

3.4.4 Crevasse geometry variation

If the width of the crevasse is larger than its height the crevasse is sufficiently shallow that it is not permitted to generate its own independent circulation (Fig. 3.11a). If the crevasse is much taller than its width, several counter-rotating circulations can form on top of each other (Fig. 3.11b). Extending the depth of the cavity below the ice shelf (Fig. 3.11c) has little effect on the qualitative nature of the flow field. A triangular shaped crevasse (Fig. 3.11d) sees a weaker freeze-driven overturning circulation, due to the narrowing of the crevasse reducing the total amount of supercooled water present at the top of the crevasse. Triangular shaped crevasses are discussed in more depth in the next section.

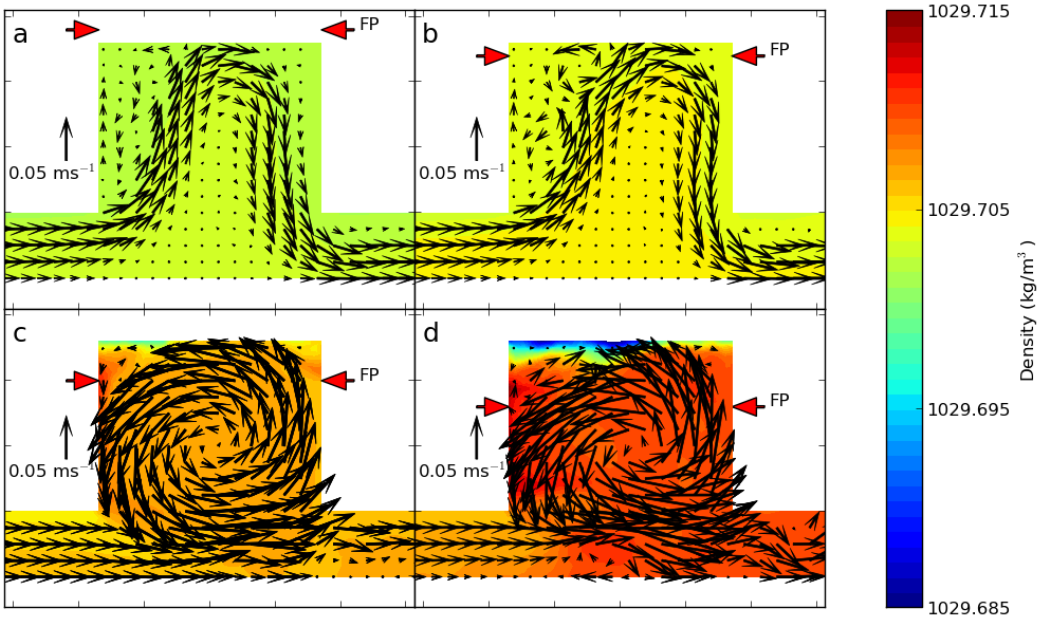

Figure 3.6: Mean density with mean velocity vectors for the inflow temperatures (a) T1, (b) T2, (c) T3 (baseline) and (d) T4. The pressure dependent freezing point (FP) of the four different inflow temperatures is also shown.

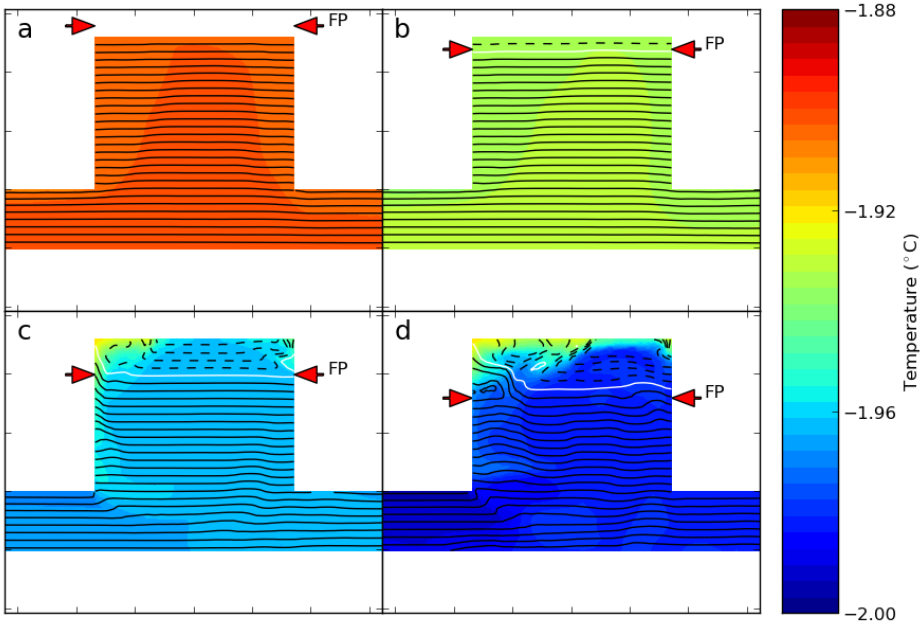

Figure 3.7: Mean temperature (colours) with thermal driving (contours) for the inflow temperatures (a) T1, (b) T2, (c) T3 and (d) T4. The white contour is at thermal driving equal to 0, while black contours are every 0.1 degree above and black dashed contours are every 0.01 degree below this point.

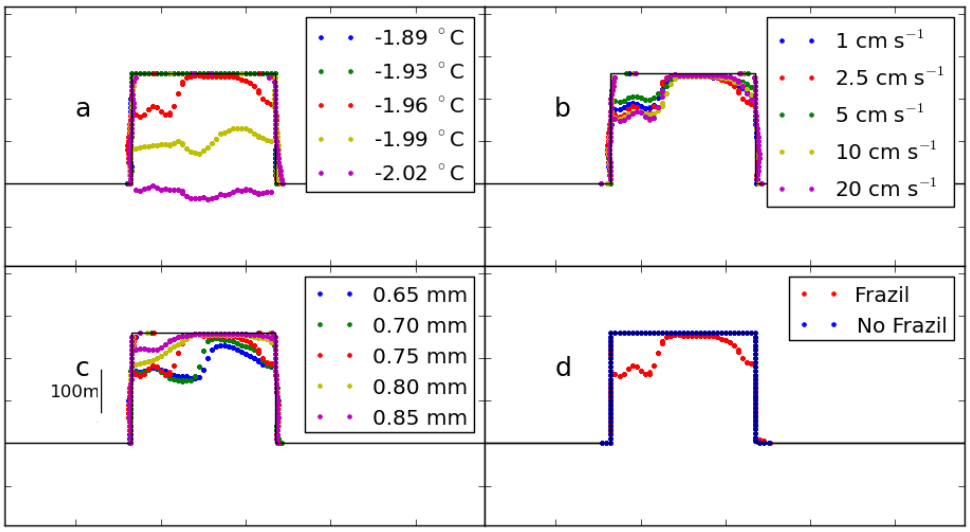

Figure 3.8: Change in crevasse geometry as a result of averaged melt rate maintained for 10 years for (a) temperature variation of inflow water, (b) velocity variation of inflow water, (c) variation in frazil crystal radii and (d) effect of no frazil component in the model. An increase in crevasse size represents melting whilst a decrease represents freezing.

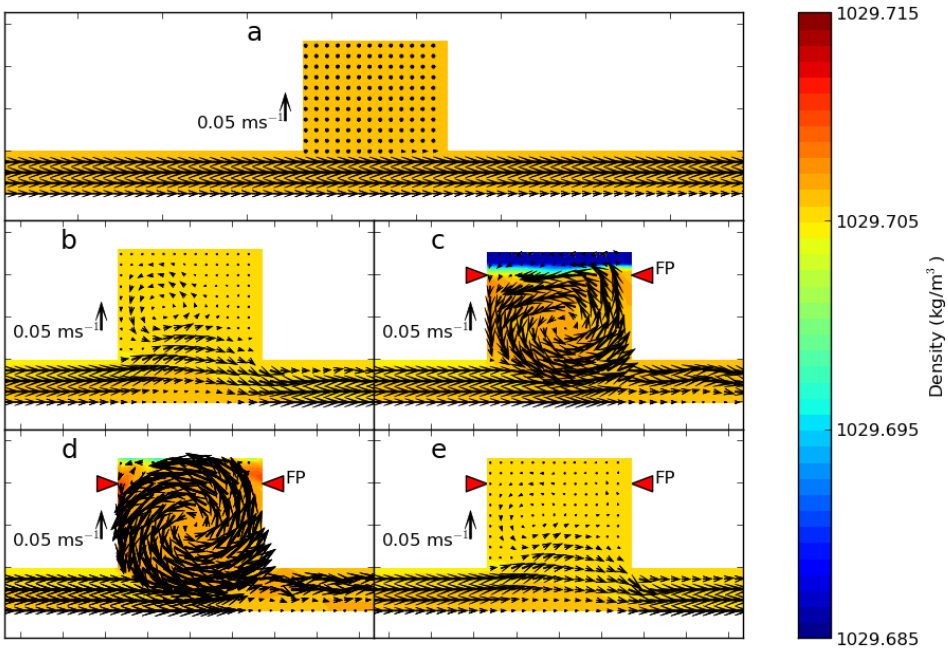

Figure 3.9: Time averaged mean density with time averaged mean velocity vectors for (a) the no-melting case, (b) the no-frazil case, (c) R025, (d) R075 (baseline) and (e) R150.

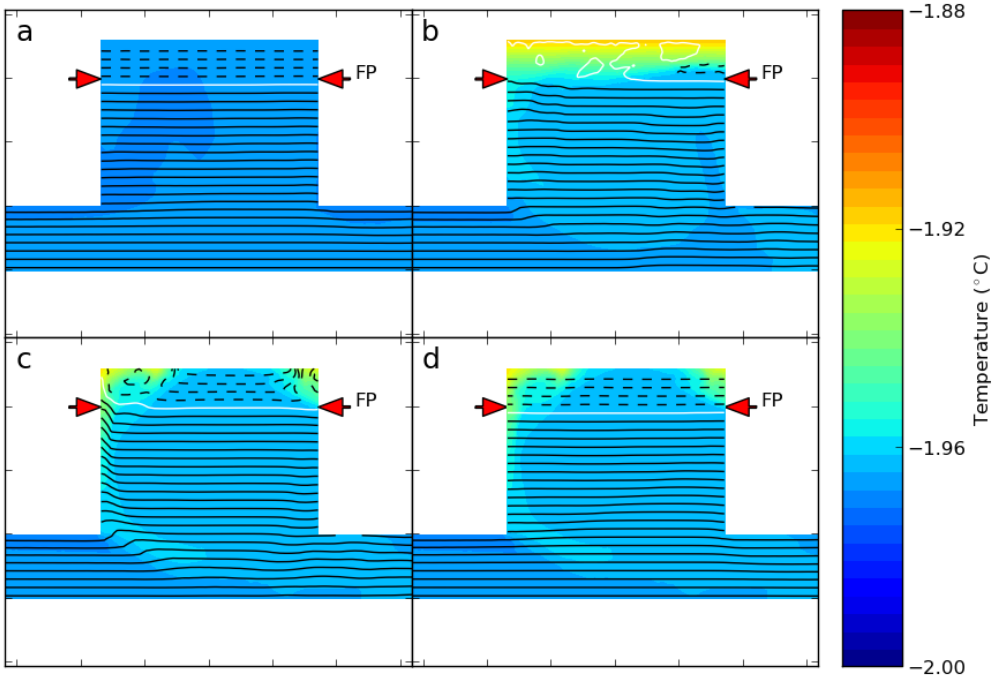

Figure 3.10: Mean temperature (colours) with thermal driving (contours) for (a) the no-frazil case, (b) R025, (c) R075 (baseline), (d) R150. The white contour is at thermal driving equal to 0, while black contours are every 0.1 degree above and black dashed contours are every 0.01 degree below this point.

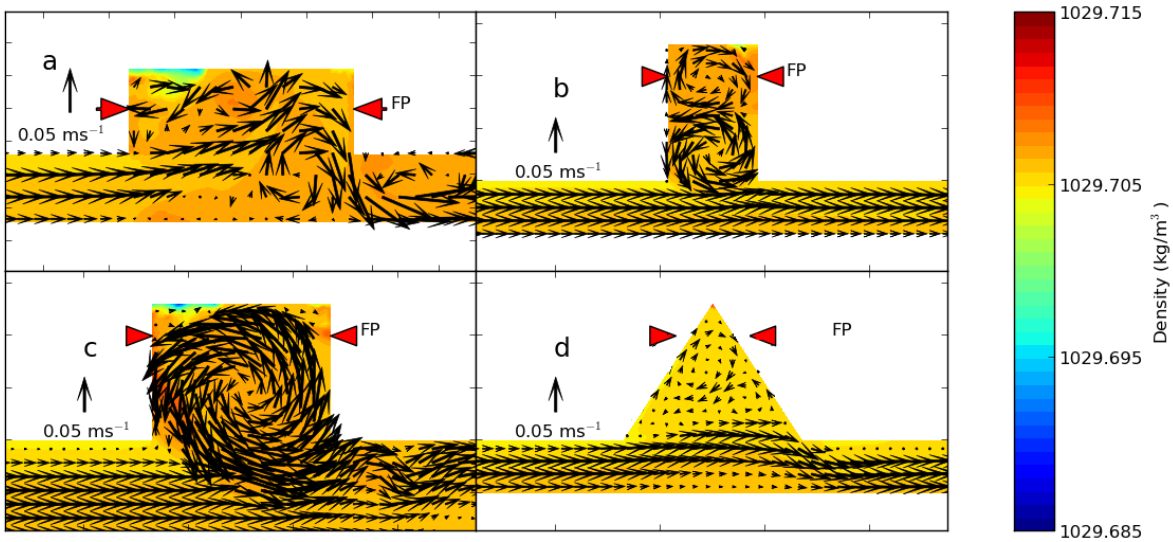

Figure 3.11: Mean density with mean velocity vectors for different crevasse geometries (a) 260 m wide and 170 m deep, (b) 130 m wide and 340 m deep, (c) cavity extended to 200 m deep and (d) cavity extended to 500 m deep.

3.5 Triangular crevasses

Observations of basal crevasses find that they tend to be triangular in nature rather than the rectangular 'rift' case the model has been calibrated against (*McGrath et al.*, 2012b). As such the results from Fig. 3.11 are expanded upon here with a comparison to the baseline case (Fig. 3.5). While the results are initially similar they are some differences that arise from the fact that the triangular shape of the crevasse limits the total amount of supercooled water present when compared to the rectangular crevasse. The circulation within the crevasse is still present, but is slower due to the reduced amount of dense water formation resulting from the limited amount of supercooled water present (Fig. 3.12a). The direction of the circulation is opposite to the baseline case, rising on the upstream side and falling on the downstream side. This is again due to the limited amount of supercooled water, making the baseline triangular case more resemble the melting dominated rectangular cases. Another consequence of the relatively smaller amount of supercooling present is that, unlike the rectangular case, the contours of equal thermal driving are not sloped but are nearly level (Fig. 3.12b). Frazil ice is concentrated on the top of the downstream side of the crevasse (Fig. 3.12c), which has the effect of concentrating freezing in the same location (Fig. 3.12d). The asymmetrical freeze pattern seen in the rectangular case is not seen here and the crevasse top fills in rapidly.

3.5.1 Long term ocean stabilisation of crevasses

Basal crevasses also have a tendency to widen as they propagate towards the calving front (*McGrath et al.*, 2012b), though it is unclear whether this is a result of melting within the crevasse or ice shelf dynamics. To investigate whether ocean driven melting of a crevasse could be responsible for their widening a comparison is made

between the averaged melt rate inside the crevasse normal to the crevasse wall and the averaged melt rate outside the crevasse. This 'melt ratio' is defined as being the ratio of the melting inside the crevasse to the melting outside the crevasse in an area 1000 m either side of the crevasse (Fig. 3.13). A melt ratio of > 1 represents a crevasse that is melting faster than surrounding ice (thus growing), a ratio < 1 but > 0 represents a crevasse that is melting quicker outside the crevasse than inside, whilst a negative melt ratio represents a crevasse that is freezing. Model simulations are run to determine the effect of varying ocean temperature, inflow velocity, crevasse depth and crevasse width.

Parameters are varied around a baseline case with inflow velocity at 0.025 m s^{-1} and water temperature at 1°C. The crevasse is triangular in shape with a depth and width of 300 m. All parameters except the one under investigation are held constant. In the temperature varying cases we could not determine any temperature where the crevasse is widening (Table 3.3). As the temperature increases the melt ratio is increasing towards the critical value of 1 but it never exceeds 1 and in any case these temperatures are far warmer than those observed under cold water ice shelves, such as Larsen C, where crevasses have been observed. By increasing the inflow velocity the melt ratio is reduced, as the crevasse fills with stagnant melt water which in turn reduces the velocity which drives the crevasse melt rate. Varying the depth (Table 3.5) and width of the crevasse (Table 3.6) has virtually no effect upon melt ratio.

Combined with the earlier results this means that the ocean can not be solely responsible for the observed widening of crevasses. For the ocean to be solely responsible for the widening of crevasse than one of two things needs to occur; either the area inside the crevasse must melt faster than the crevasse itself or the area outside the crevasse must freeze quicker than the crevasse. The former does not happen because in warm cases the crevasse fills with stagnant meltwater, limiting the flow within

Table 3.3: The effect of temperature variation on melt ratio.

Temperature (°C)	Melt ratio
-2	-0.53
-1	0.25
0	0.41
1	0.58
2	0.68
3	0.73

Table 3.4: The effect of inflow velocity variation on melt ratio.

Inflow velocity (m s^{-1})	Melt ratio
0.025	0.58
0.05	0.13
0.01	0.06
0.015	0.04

the crevasse. The latter does not occur because in cold cases the depth dependency of freezing will always result in more freezing higher up in the crevasse than outside. As crevasses are a common feature on the undersides of ice shelves there must be some ice-dynamical mechanism responsible for maintaining crevasses in the face of melt-driven erosion or marine-ice filling.

Table 3.5: The effect of crevasse depth on melt ratio.

Depth (m)	Melt ratio
300	0.58
100	0.57

Table 3.6: The effect of crevasse width on melt ratio.

Width (m)	Melt ratio
100	0.59
200	0.58
300	0.58

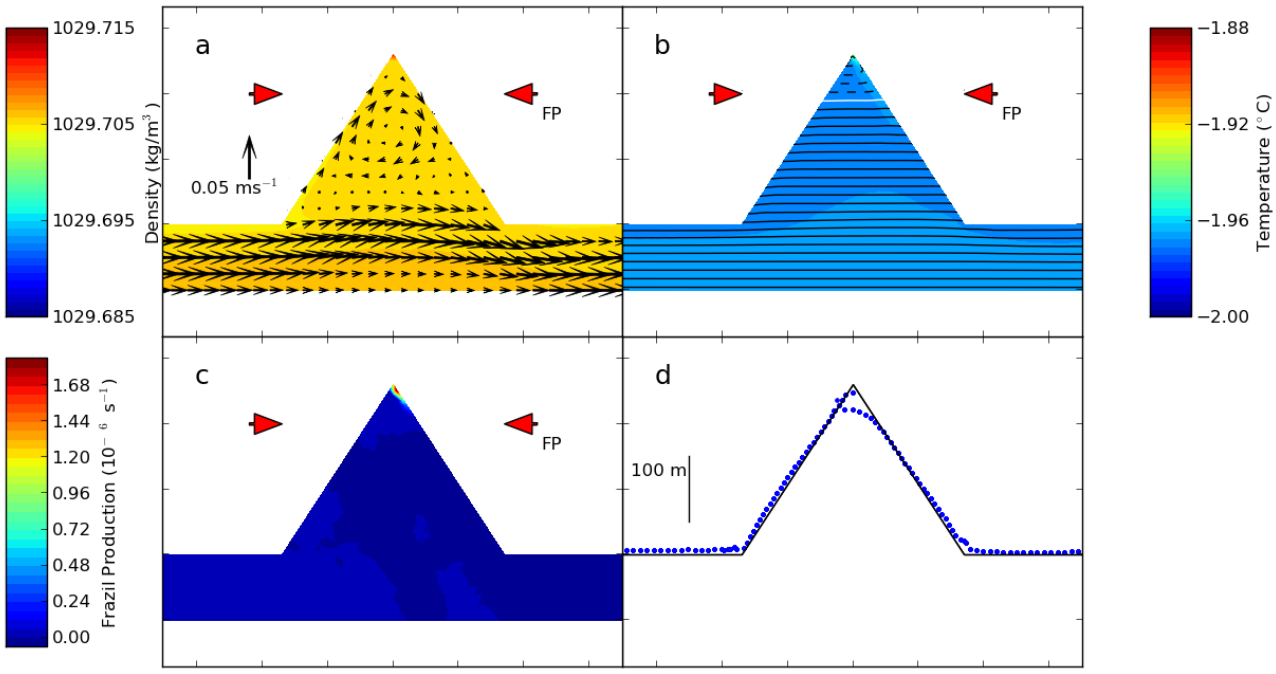

Figure 3.12: Triangular crevasse with the same set up parameters as the baseline case showing (a) time-averaged mean density with mean velocity vectors, (b) mean temperature (colours) with mean thermal driving (contours), (c) mean frazil crystal production and (d) change in crevasse geometry as a result of mean melt rate maintained for 5 years. The white contour in panel b is at zero thermal driving while black contours are every 0.1 degree above and black dashed contours are every 0.01 degree below this point. The pressure dependent freezing point (FP) of the water properties used for initial and inflow conditions is also shown.

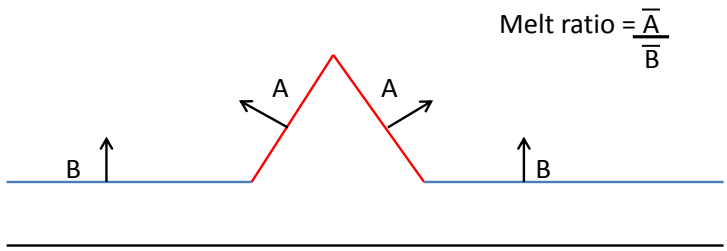

Figure 3.13: Definition of melt ratio. The melt ratio is equal to the mean melt rate of the inside walls of the crevasse in the direction perpendicular to the wall (A) divided by the mean melt rate of the outside the of the crevasse (B).

3.6 Conclusions

Fluidity has been used to study the circulation and ice-ocean interaction in an idealised, two-dimensional ice shelf basal crevasse. The following conclusions are drawn:

1. Circulation within a crevasse is highly dependent upon the amount of freezing. Two different circulation patterns are found, one freeze dominated and one melt-dominated. In the first an unstable overturning circulation is formed due to dense water formation at the top of the crevasse, whilst in the second a stable melt water layer is formed along the sides and top of the crevasse. Which circulation is present is determined by the amount of freezing taking place in the crevasse, with the melt-driven circulation for low amounts of freezing and the freezing-driven case otherwise. In the absence of melting and freezing there is essentially no flow in the crevasse.

2. Frazil ice precipitation is the dominant factor in the freeze rate within basal crevasses, providing roughly 99% of the freeze rate in the baseline case. At lower amounts of supercooling direct freezing becomes more important, although frazil ice precipitation is still the prime means of freezing. Frazil ice formation is largely determined by ocean temperature and crystal radius, with higher ocean velocities providing only a small increase in freezing. Future modelling studies of ice shelves with basal crevasses therefore need to be aware of the crucial role played by frazil ice.

3. Freezing in the crevasse is primarily dependent upon the temperature of the inflow water and the chosen size of the model's 'representative' frazil crystal radius, with inflow velocity having a much smaller effect. Use of a multiple size class frazil model would reduce the dependency on frazil crystal radius, and would be a logical first step for future model improvements. There is a nonlinear relationship between

inflow temperature and freezing rate, with temperatures 0.03 ° C colder than the baseline case quickly approaching freezing rates of 50 m a year. As such, it is considered highly unlikely that much more than 60 m of supercooling would be present in a basal crevasse, as otherwise it would quickly fill with marine ice. The rapid freezing permitted by frazil ice creates a strong asymmetry where crevasses can fill with marine ice after a cooling far more rapidly then the marine ice would be eroded after a similar warming.

4. Oceanic forcing can not be solely responsible for widening of basal crevasse. For this to happen the ice shelf outside the crevasse must either melt at a slower rate or freeze at a faster rate when compared to the inside of the crevasse. This does not happen due to stagnant meltwater restricting flow in a crevasse in the former and the pressure dependency of freezing in the latter.

Freezing in ice shelf crevasses provides a strong stabilising influence on ice shelves underlain by cold water that is not found elsewhere, and frazil ice deposition is the dominant means by which this occurs.

4 The conditional instability of frazil ice in seawater

4.1 Overview

This chapter is an investigation into the conditional instability of frazil ice growth in seawater, and the majority of the work presented in this chapter has been published in *Journal of Physical Oceanography* as *Jordan et al.* (2015). It has been suggested that the presence of frazil ice can lead to a conditional instability in seawater. Any frazil forming in the water column reduces the bulk density of a parcel of frazil-seawater mixture, causing it to rise. Due to the pressure-decrease in the freezing point, this causes more frazil to form, causing the parcel to accelerate, and so on. Frazil ice formation requires a "seed" (another frazil ice crystal, grain of sediment, etc.) for nucleation to occur. Throughout this work such seeds are assumed to be always present, allowing nucleation to occur anywhere water is below its local freezing point. The model set up described in Chapter 2 is used to examine how this system evolves over time, focusing on the density perturbation expressed as an initial frazil ice concentration. The model is then used to investigate frazil ice growth in a scenario representing an ISW outflow from beneath an ice shelf. Finally, the conclusions that can can be drawn from this work are summarised.

4.2 Numerical modelling of an idealised instability

4.2.1 Model setup

ISW plumes are a mixture of frazil ice and a freshwater anomaly. This leads to a density perturbation comprised of the two, with the frazil ice instability enhancing the underlying convection where present. It is this combination of a frazil and freshwater anomaly density perturbation that is being investigated in this section. This is done by using the model described in Chapter 2.

To investigate the full conditional instability of frazil ice growth a simple, two-dimensional box model 400 m deep by 200 m wide, with a 5 m mesh resolution throughout is used. Unlike in the previous section, the water has a vertically uniform initial thermal driving $T^* = T^*_{in}$ except within the bottom 20 m, which has $T^* = 0$. A constant initial density gradient $\frac{\partial \rho}{\partial z}_{in}$ is imposed by salinity. The vertical uniform thermal driving and density gradient are a simplification for the idealised experiment; observations near ice shelves during frazil ice formation generally show depth varying thermal driving and density gradients (e.g. *Mahoney et al.*, 2011). The bottom 20 m has an initial concentration of frazil ice C_{in}, while the rest is ice-free. Zero-flux Neumann boundary conditions for scalars and no-slip boundary conditions for velocity are applied in discretised space ('weakly applied') at all boundaries except for frazil at the top boundary, which is allowed to deposit (*Jordan et al.*, 2014). As in the previous chapter a time step of 5 s has been used.

The baseline case has $C_{in} = 10^{-3}$, $T^*_{in} = 10^{-1}$ °C, $\frac{\partial \rho}{\partial z}_{in} = -10^{-5}$ kg m^{-4}, frazil crystal radius r=0.75 mm and diffusivity K of 10^{-3} m^2 s^{-1} (Fig. 4.1). A sensitivity study around this baseline was carried out for a range of thermal drivings (T^*_{in}=10^{-2}

to 1 °C), density gradients ($\frac{\partial \rho}{\partial z}_{in} = -10^{-3}$ to -10^{-6} kg m^{-4}), frazil crystal radii (r=0.25 and 1.25 mm), diffusivities/viscosities (K=10^{-1} and 10^{-5} m^2 s^{-1}) and initial frazil ice concentrations (C_{in}=2×10^{-3} and 5×10^{-4}). For the sensitivity study all parameters except the one under investigation are held at their baseline value. In the baseline case the frazil concentration reached a maximum after 12 hours and so model runs in the sensitivity study were carried out for this time. At the end of a run the total amount of frazil ice suspended in the water column and deposited on the top boundary is recorded. A stable case is deemed to be one where there is no frazil ice at the end of the run, while an unstable case one in which frazil ice is present.

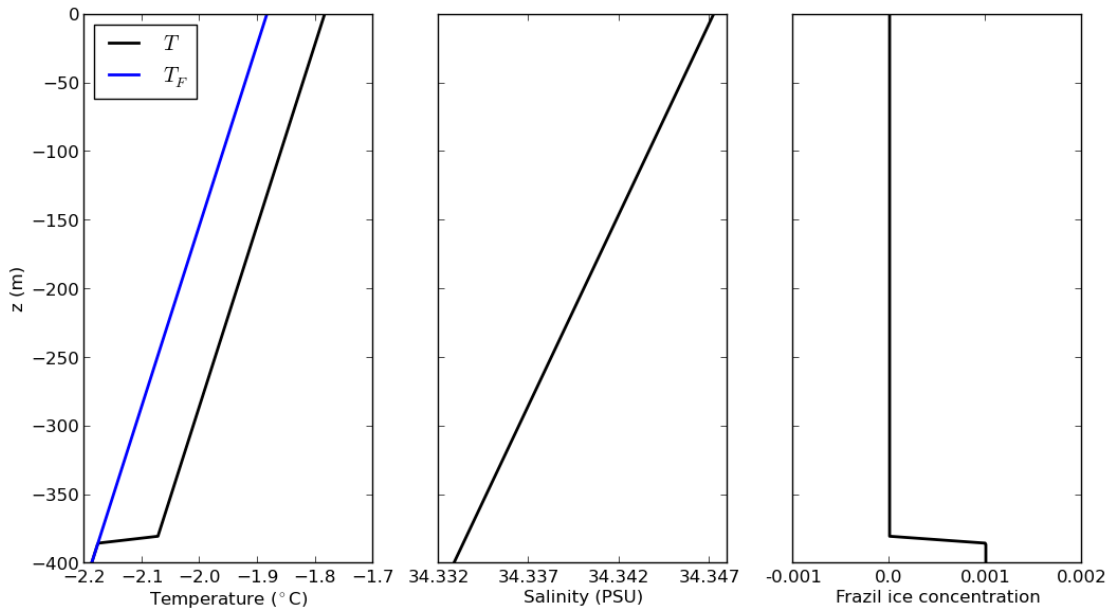

Figure 4.1: Idealised non-hydrostatic ocean model setup. Initial profiles for the baseline case (T^*_{in}=10^{-1} °C, $\frac{\partial \rho}{\partial z}_{in} = -10^{-5}$ kg m^{-4}, $C_{in} = 10^{-3}$, $r = 0.75$ mm and $K = 10^{-3}$ m^2 s^{-1}) of (a) T (black) and T_F (blue), (b) S and (c) C.

ISW plumes in nature are a mixture of a freshwater anomaly and frazil ice. For simplicity the freshwater perturbation is not provided explicitly in the simulations, but this perturbation is implicitly present in the choice of frazil perturbation C_{in}. In the setup, if the frazil melts then the meltwater drives a conventional gravitational instability, which may or may not then be assisted by frazil regrowth. Due to the role of a freshwater anomaly this is a 'mixed' instability. The effect of this choice is investigated by also manufacturing a 'pure' frazil instability by salt-compensating the initial frazil concentration such that if all the frazil were to melt instantaneously, there would be no initial density perturbation.

4.2.2 Results

The evolution of the instability in the base case is shown in Fig. 4.2. The initial density perturbation (defined as ρ_{in}, the initial density, minus ρ, the density of the ice-seawater mixture) coalesces into separate 'blooms' which merge as they rise. The maximum local density perturbation decreases in strength from around $t = 900$ s until it recovers at around t=4500 s, which is associated with a decline and re-establishment of the frazil. The density perturbation is largely manifested as a freshwater anomaly perturbation during $t = 1800 - 3600$ s. The interplay between density, thermal driving and frazil ice concentration allows the growth of the instability, even if it is only manifested in frazil after $t = 4500$ s. The largest density perturbations are caused by frazil ice, as illustrated by the density perturbation being present even when there is a positive salinity anomaly (e.g. $t = 5400$ s).

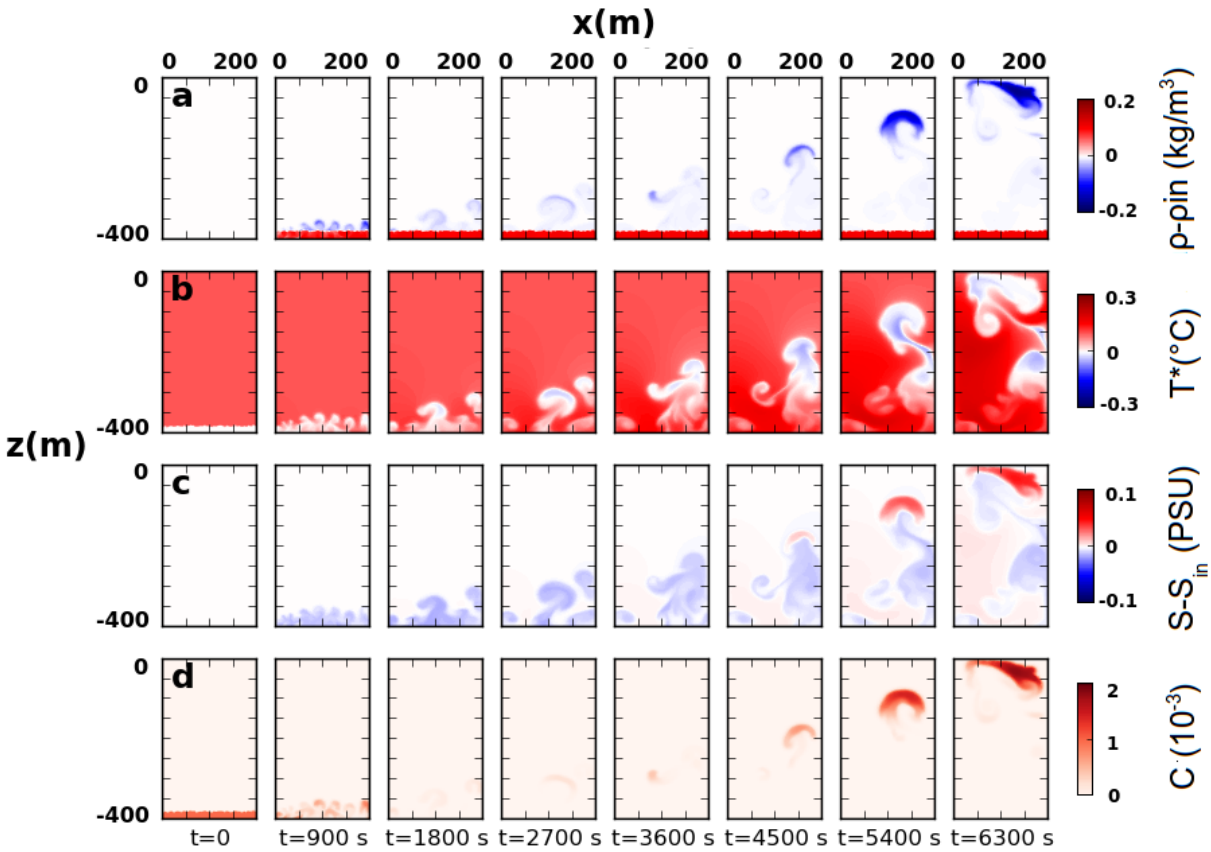

Figure 4.2: Results of the idealised non-hydrostatic ocean model setup. The instability for the unstable baseline case (T^*_{in}=10^{-1} °C, $\frac{\partial \rho}{\partial z}_{in} = -10^{-5}$ kg m^{-4}, $C_{in} = 10^{-3}$, $r = 0.75$ mm and $K = 10^{-3}$ m^2 s^{-1}) in terms of (a) density relative to initial density, (b) thermal driving, (c) salinity relative to initial salinity and (d) frazil ice concentration.

The instability can be suppressed in a number of ways (Fig. 4.3). These stable cases initially progress similarly to the unstable case (Fig. 4.3a), but following the initial melting of the frazil ice the density perturbation never re-establishes itself. In the stratification-limited case, the perturbation does not rise fast enough to overcome the frazil melting given by the thermal driving (Fig. 4.3b). In the thermally-limited case the thermal driving is too strong to be overcome by freezing-temperature change even if the parcel is rising relatively quickly (Fig. 4.3c). The increased temperature also reduces the relative magnitude of the initial density perturbation. Warming decreases the initial density perturbation because the bottom 20 m is held at the freezing temperature while the rest of the domain is warmed. In this particular case the frazil-seawater mixture is lighter than the warmer water, but the equivalent freshwater anomaly is not, so once the ice melts the instability is suppressed (see below). In the mixing-limited case the perturbation follows the evolution of the stable case initially but the density anomaly decreases because the background mixing erodes the negative density anomaly faster than it can rise (Fig. 4.3d).

This section considers a combined frazil-freshwater anomaly ice instability. To illustrate the role of frazil, a 'pure' frazil instability can be simulated by setting an initial salt perturbation in the bottom 20 m of the model domain that precisely offsets the freshwater anomaly input that would arise from the melting of the initial frazil ice. In this case the density anomaly driving the instability is purely from frazil ice growth, and the instability does not cause increased frazil ice (Fig. 4.3e). Therefore it is concluded that in the baseline case the frazil is actually assisting an underlying gravitational instability.

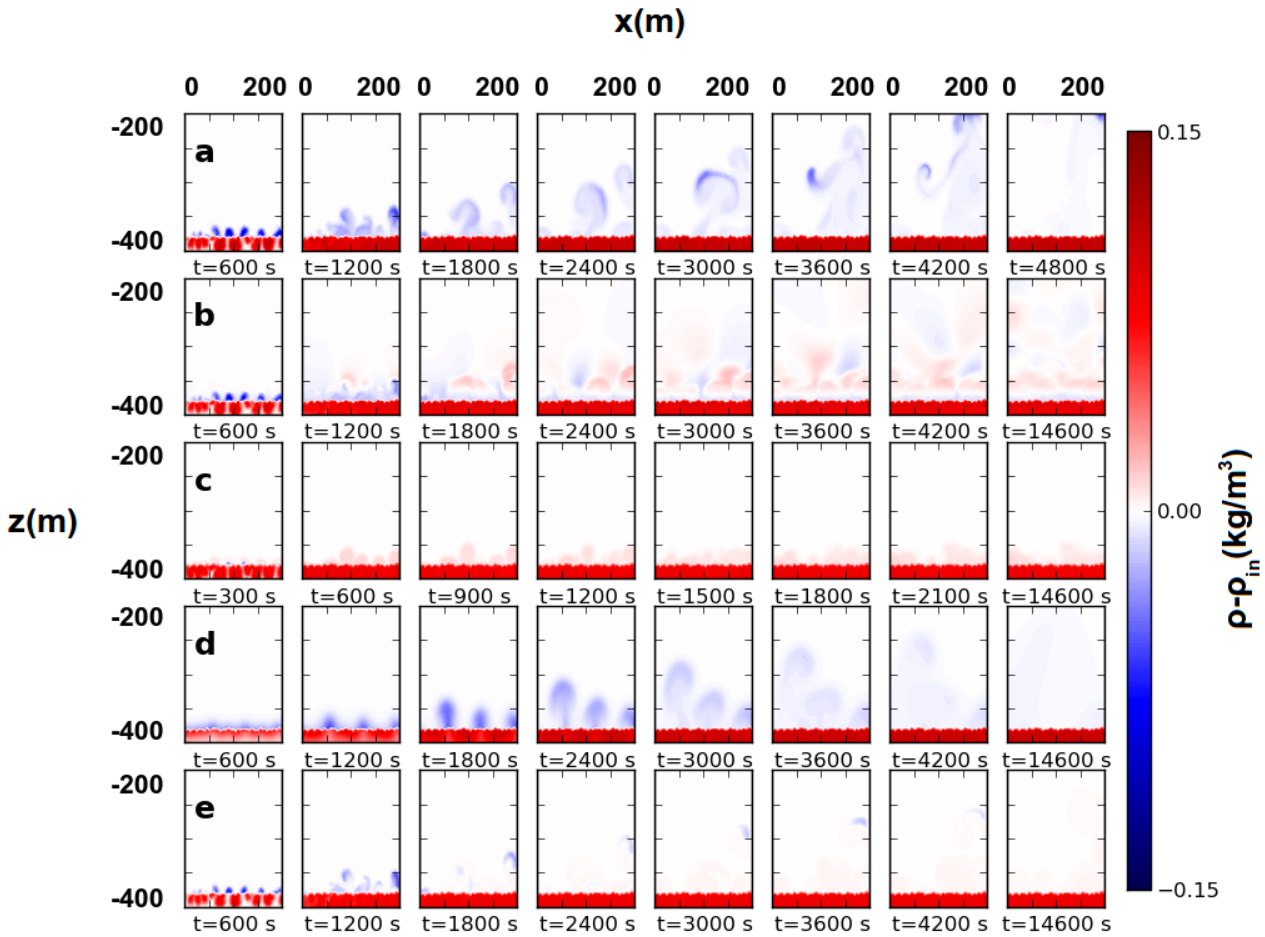

Figure 4.3: Results of the idealised non-hydrostatic ocean model setup. Panels show the density relative to the initial density of (a) the baseline case (T^*_{in}=10^{-1} °C, $\frac{\partial \rho}{\partial z}_{in} = -10^{-5}$ kg m^{-4}, $C_{in} = 10^{-3}$, $r = 0.75$ mm and $K = 10^{-3}$ m^2 s^{-1}) and also cases for which the instability is limited by (b) stratification ($\frac{\partial \rho}{\partial z}_{in} = -10^{-3}$), (c) thermal driving ($T^*_{in}$=1°C), (d) background mixing ($K = 10^{-1}$ m^2 s^{-1}) and (e) salinity compensated case where the salinity in the bottom 20 m has been increased by an amount equal to melting the initial frazil ice concentration. Note the different time axes.

The thermal stabilisation of the baseline case (Fig. 4.3c) is a result of the combination of warming prohibiting frazil ice formation and also reducing the initial density perturbation. If the density difference caused by the warming is compensated by a freshening in the bottom 20 m, pure thermal suppression of the frazil instability can be shown (Fig. 4.4). In contrast to the baseline case the density perturbation does not grow in size, but reduces in magnitude as the water rises (Fig. 4.4a). The density perturbation does not rise fast enough to overcome the warming and never freezes (Fig. 4.4b). The density perturbation in this particular case is driven solely by a freshwater anomaly, as can be seen in the negative salinity anomaly (Fig.4.4c) and lack of frazil ice (Fig. 4.4d). This case is gravitationally unstable, but the growth of frazil ice is stabilised by the thermal driving.

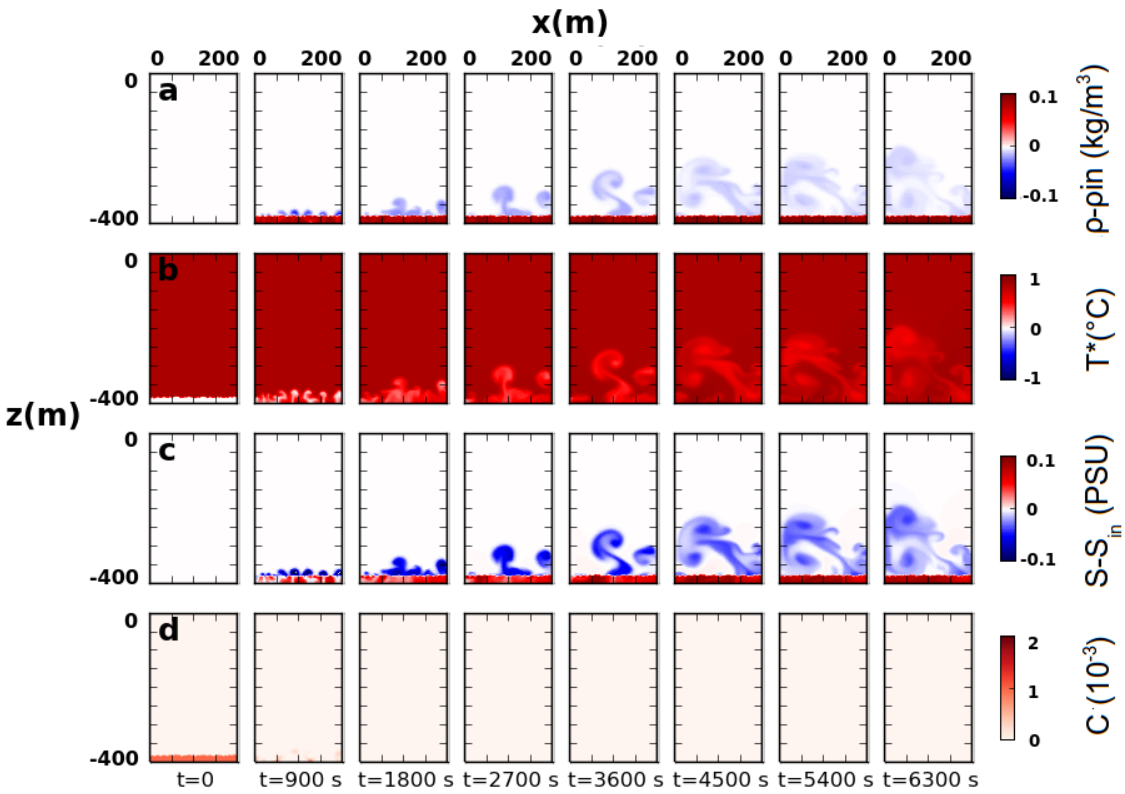

Figure 4.4: Results of the idealised non-hydrostatic ocean model setup. The instability for the purely thermally stable case (T^*_{in}=1°C, $\frac{\partial \rho}{\partial z}_{in} = -10^{-5}$ kg m^{-4}, $C_{in} = 10^{-3}$, $r = 0.75$ mm and $K = 10^{-3}$ m^2 s^{-1} with salinity in the bottom 20 m reduced to compensate the 1°C warming of the rest of the domain) in terms of (a) density of the combined frazil-seawater mixture relative to the initial density, (b) thermal driving, (c) salinity relative to initial salinity and (d) frazil ice concentration.

The effect of varying thermal driving and density gradient upon overall frazil ice growth whilst initial frazil ice concentration, background mixing and frazil crystal radius are held constant is shown in Fig. 4.5. The results are linearly interpolated between the set of discrete runs marked in white, with the white contour showing where the initial amount of frazil ice is the same as that at the end of the model run. Significant instabilities are found forming in water that is initially above freezing. Decreasing the density gradient much beyond $\frac{\partial \rho}{\partial z}_{in} = -10^{-3}$ kg m^{-4} or increasing thermal driving beyond T^*_{in}=10^{-1} °C suppresses the instability, either by preventing the parcel from rising or by preventing it from supercooling as it rises. The zone of instability resembles the behaviour found in the linear stability analysis (Fig. **??**a), though the results are not directly comparable due to the difference in the background conditions as well as the time scales involved. In both cases there is a zone of instability, dependent upon thermal driving, density gradient, initial frazil concentration and frazil crystal radius. The exact area of the zone of instability for thermal driving and density gradient will depend upon the values of initial frazil ice concentration, background mixing and frazil crystal radius used. A greater initial frazil ice concentration, for example, would promote the formation of the instability by lowering the necessary values of thermal driving and background mixing for the instability to be present. The general shape of the zone of instability, however, remains the same.

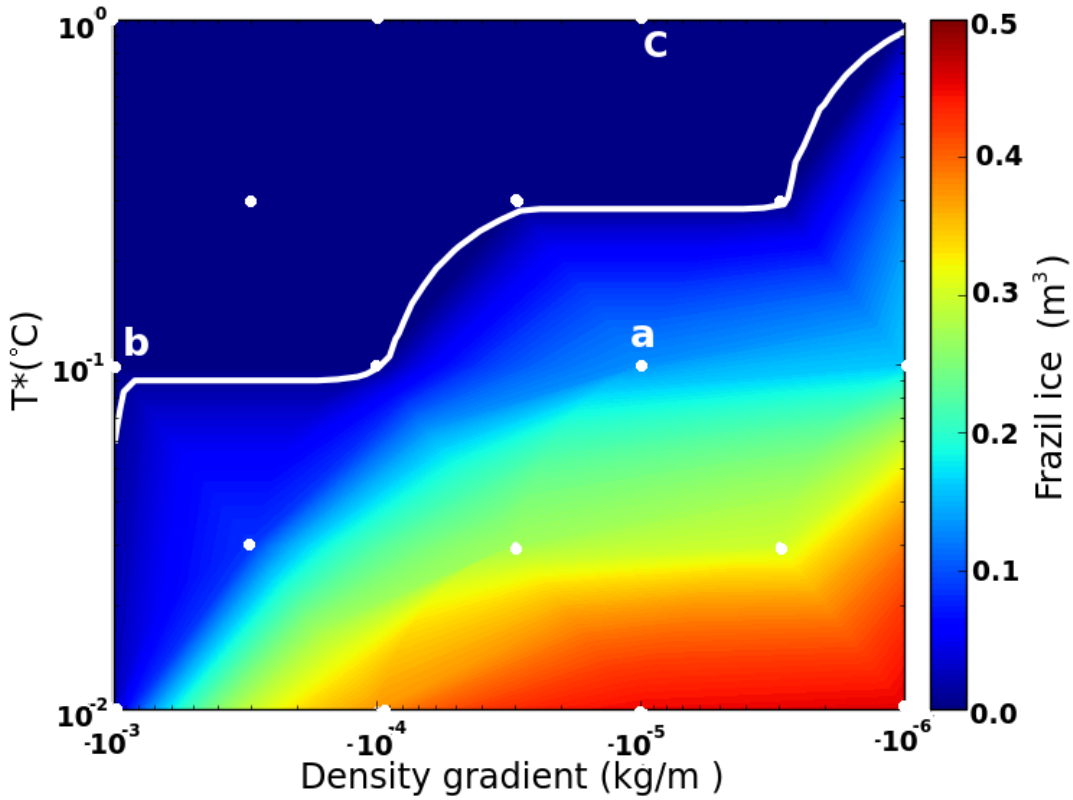

Figure 4.5: Total frazil ice at the end of the idealised non-hydrostatic ocean model simulation as a function of thermal driving and density gradient for C_{in}=10^{-3}, r=0.75 mm and $K = 10^{-3}$ m^2 s^{-1}. Model runs were carried out for the 18 combinations of T^*_{in} and $\frac{\partial \rho}{\partial z}_{in}$ marked in white, with results linearly interpolated between. The white contour shows where the initial frazil ice concentration is the same as the final frazil ice concentration (note logarithmic scale). The final locations of the (a) the baseline, (b) the stratification-limited cases and (c) the thermal-driving limited shown in Fig. 4.3 are marked.

The sensitivity of the results to higher and lower temperatures (T^*_{in} = 1 °C, T^*_{in} = 10^{-2} °C), stratification ($\frac{\partial \rho}{\partial z}_{in} = -10^{-3}$ kg m^{-4}, $\frac{\partial \rho}{\partial z}_{in} = -10^{-6}$ kg m^{-4}), frazil crystal radius (r = 0.125 mm, r= 0.25 mm), background mixing (K =10^{-1} m^2 s^{-1}, K=10^{-5} m^2 s^{-1}), initial frazil concentration (C_{in}= 2×10^{-3}, C_{in}= 5×10^{-2}), frazil rise velocity (w_i = 0 m s^{-1}) and the previously discussed 'pure' (salinity compensated) case is shown in Fig. 4.6. The baseline case can be separated into two phases, the first being an initial period of melting while the frazil ice is coalescing into a bloom (Fig 4.6a) and the second a period of freezing as the bloom rises (Fig. 4.6b).

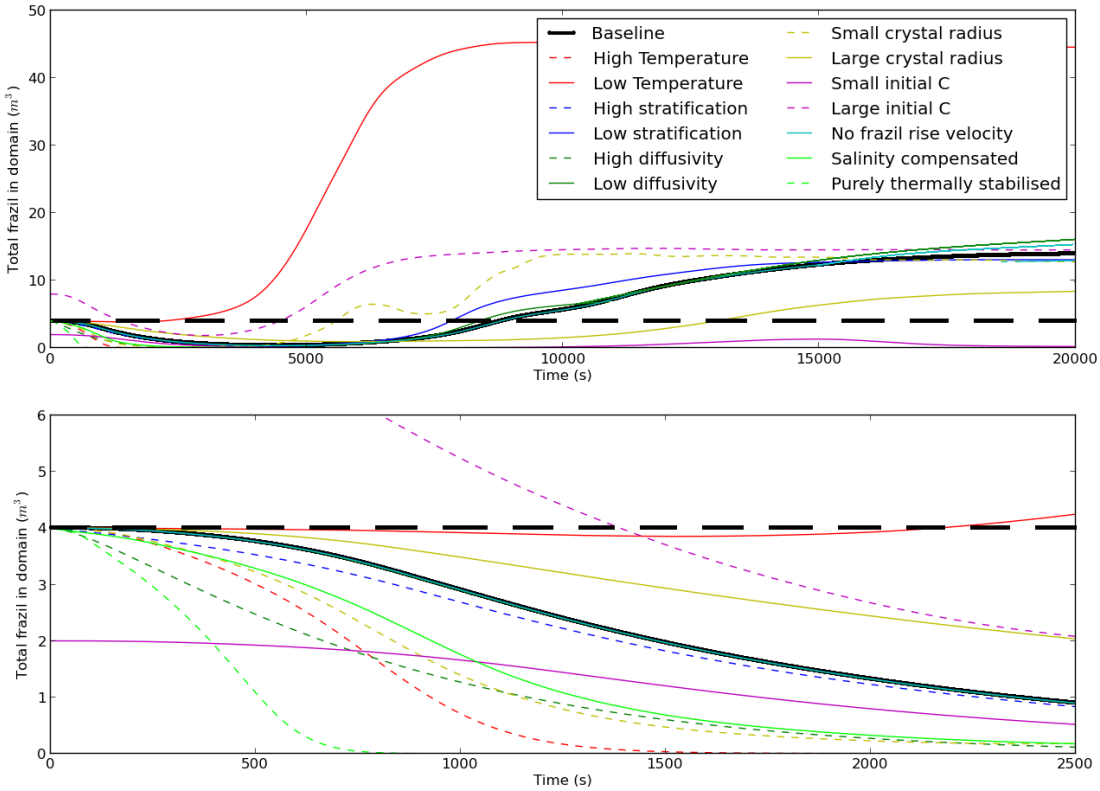

Figure 4.6: Evolution of total frazil ice in the idealised non-hydrostatic ocean model for (a) the full 20000 s of the model run and (b) the first 2500 s. The baseline case (T^*_{in}=10^{-1} °C, $\frac{\partial \rho}{\partial z}_{in} = -10^{-5}$ kg m^{-4}, $C_{in} = 10^{-3}$, $r = 0.75$ mm and $K = 10^{-3}$ m^2 s^{-1}) is shown, and the black dashed line shows the amount of frazil ice at the start of the simulation. Also shown are the results of varying higher and lower temperatures ($T^*_{in} = 1$ °C, $T^*_{in} = 10^{-2}$ °C), stratification ($\frac{\partial \rho}{\partial z}_{in} = -10^{-3}$ kg m^{-4}, $\frac{\partial \rho}{\partial z}_{in} = -10^{-6}$ kg m^{-4}), frazil crystal radius (r = 0.125 mm, r= 0.25 mm), K (10^{-1} m^2 s^{-1},10^{-5} m^2 s^{-1}) C_{in}, initial frazil concentration (C_{in}= 2×10^{-3} and C_{in}= 5×10^{-2}), salinity compensated case (where salinity in the bottom 20 m has been increased to directly offset the freshwater anomaly gained from melting the initial frazil ice concentration), pure thermally stableaised case (where salinity in the bottom 20 m has been reduced to off set the density change arise from the increase in thermal driving of the rest of the domain) and frazil rise velocity ($w_i = 0$ m s^{-1}) whilst keeping all other parameters at their baseline values.

The results are highly sensitive to temperature, with lower values of T_{in}^* showing a rapid increase of frazil ice with only a small fraction of the initial melting seen in the baseline case. High T_{in}^* cases rapidly melt the frazil ice, both in the baseline thermally stabilised case and the solely thermally stabilised case. Varying the density stratification has little impact on the initial melting period, but it does affect how quickly the frazil ice can rise and so impacts the freeze period. The low-stratification case shows an increased rate of freezing during this period, whilst the high-stratification case shows no freezing because the frazil-seawater mixture is unable to rise. The frazil crystal radius affects the rate at which the individual crystals freeze or melt, with larger crystals both melting and freezing slower than the baseline case due to the decreased ratio of surface area to volume. This can be seen in the delay of the onset of the freezing period, with the inverse true for the smaller frazil crystal radii. Increasing the diffusivity makes it harder for the frazil concentration to reach the critical volume needed for a buoyant bloom. Reducing the diffusivity has little impact on the results. By reducing the initial frazil concentration, and thus reducing the perturbation, it is possible to shut down the instability as there is less initial buoyancy forcing driving the frazil rising. Similarly, increasing the initial concentration reduces the time needed for the instability to grow ice due to the increase of the initial buoyancy forcing. In the salinity compensated case the size of the initial density perturbation and buoyancy forcing has been reduced, shutting down the instability in a similar way to the smaller initial concentration case. Finally, by disabling the frazil rise velocity only a very slight increase in final frazil ice is seen.

4.3 Numerical modelling of an Ice Shelf Water outflow

4.3.1 Model setup

Having investigated the combined frazil-freshwater anomaly instability in a simple box model Fluidity is now used to consider the suspended frazil ice observed in front of ice shelves in Antarctica. The area in front of an ice shelf is modelled by means of a two-dimensional domain 400 m deep by 2500 m wide, with a 20 m mesh resolution used throughout (Fig. 4.7). Ignoring the effects of rotation is justified in that, assuming a typical ice shelf around Antarctica is at 70^0 South, the Rossby radius of deformation is of the order of 3500 km. The water has a constant initial thermal driving and a density gradient imposed by salinity. Diffusivities/viscosity of $K = 10^{-3}$ m^2 s^{-1} are used. The top 300 m of the left boundary represents the front of an ice shelf with the bottom 100 m the cavity underneath. The right boundary represents the ocean, the top boundary is the sea surface and the bottom boundary is the sea bed. An inflow (U_{in}) enters the domain at the bottom of the left side (x=0) under steady Dirichlet boundary conditions ($u = U_{in}$, $w = 0$, $T^* = 0$, $S = S_{in}$ and $C = 0$) and leaves via the bottom 100 m of the right side (x=2.5 km) with zero-flux Neumann boundary conditions. By limiting the outflow to the bottom 100 m of the water column it is ensured that rising water is caused solely by the frazil instability as the inflow water leaves at the same depth at which it enters the domain. The instability is 'pure' in the sense that there is no initial density anomaly, all frazil ice within the model is generated by the instability. No-slip boundary conditions are applied in discretised space ('weakly applied') at all other boundaries. Zero-flux conditions for heat, salt and frazil are applied at the seabed, top and sides. The one exception to this is that frazil is allowed to deposit at the top and leave via the right

hand boundary. The total amount of frazil ice depositing on the top of the model domain is recorded after 24 hours of simulation time.

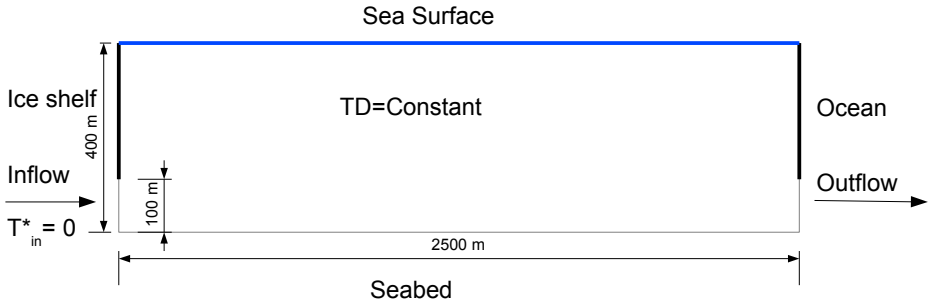

Figure 4.7: Schematic of non-hydrostatic ice-shelf model setup. An inflow enters the domain from the bottom 100 m on the right-hand side and leaves via the bottom 100 m on the right-hand side. The inflow water is at the freezing temperature, whilst the rest of the domain has a constant thermal driving. No frazil is present in the inflow or initial conditions.

4.3.2 Results

The evolution of a frazil ice 'bloom' within the domain for the unstable baseline case (T^*_{in}=10^{-2} °C, $\frac{\partial \rho}{\partial z}_{in} = -10^{-6}$ kg m^{-4}, $r = 0.75$ mm, $K = 10^{-3}$ m^2 s^{-1} and $U_{in} = 0.05$ m s^{-1}) is shown in Fig. 4.8. As the inflow water is at the local freezing temperature, any upwards motion will cause frazil ice to form, though whether this is sufficient to create an instability depends on the factors previously discussed. Unlike in the previous section the density perturbation is always dominated by frazil ice due to the initial conditions; there is no period during which it is expressed as a freshwater anomaly. The inflow causes a large amount of supercooling as it rises. Once the 'bloom' of frazil ice begins at $t = 13800$ s there are corresponding areas of descending, salty waters. As before, frazil concentration has a greater effect on density than the salinity anomaly caused by freezing.

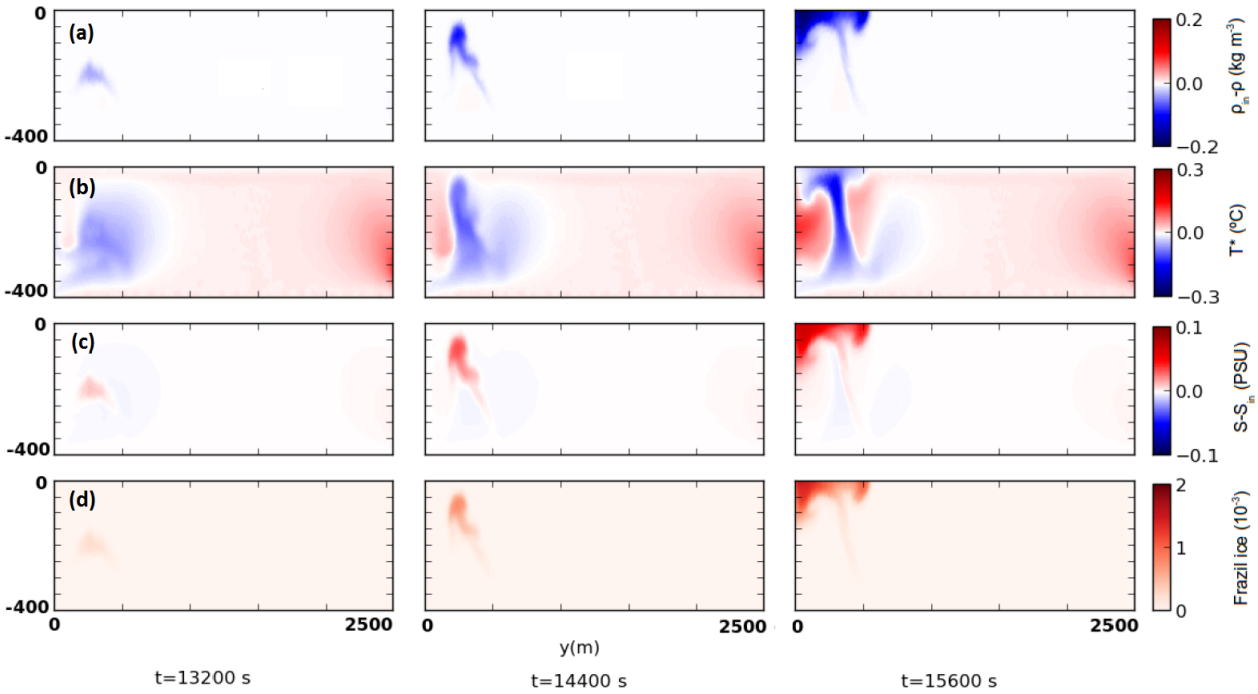

Figure 4.8: Evolution of frazil ice growth in the non-hydrostatic ice shelf model for the baseline case (T^*_{in}=10^{-2} °C, $\frac{\partial \rho}{\partial z}_{in} = -10^{-6}$ kg m^{-4}, $r = 0.75$ mm and $K = 10^{-3}$ m^2 s^{-1}) in terms of (a) density relative to initial density, (b) thermal driving, (c) salinity relative to initial salinity and (d) frazil ice concentration.

The dependence of mean frazil deposition on density gradient and thermal driving over the domain (whilst background mixing and frazil crystal radius are held constant) is shown in Fig 4.9. There is a strong agreement with the earlier results (Fig. 4.5), in that density gradients greater than $\frac{\partial \rho}{\partial z}_{in} = -10^{-3}$ kg m^{-4} and thermal driving greater than T^*_{in}=10^{-1} °C will shut down the instability. The results are linearly interpolated between the set of discrete runs marked in white, with the white contour showing the line of zero frazil deposition. As before the exact area of the 'zone of instability' will vary with the frazil crystal radius and background mixing, but the general shape should remain the same. Mean frazil ice deposition at the sea surface is of the order of 0.1 m/day, a highly significant amount compared to typical growth rates of sea ice in winter.

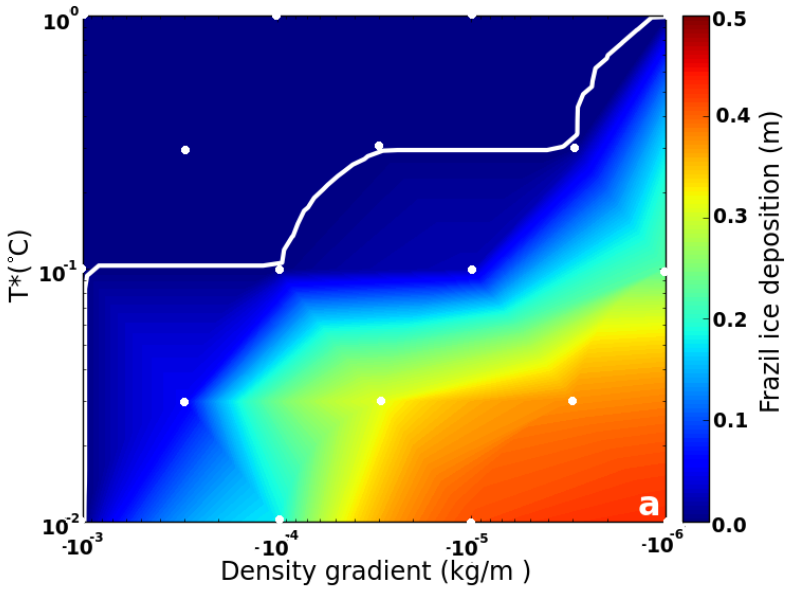

Figure 4.9: Results of the non-hydrostatic Ice Shelf Water model setup. Spatial mean frazil ice deposition after 24 hours as a function of thermal driving and density gradient for $r = 0.75$ mm and $K = 10^{-3}$ m^2 s^{-1}. Model runs were carried out for combinations of T^*_{in} and $\frac{\partial \rho}{\partial z}_{in}$ marked in white, with results linearly interpolated between. The white contour shows the zero deposition contour. The location of (a) the baseline case is shown.

The baseline case is used for a sensitivity study, with all parameters except the one under investigation held constant. Fig. 4.10 shows the total amount of frazil ice deposited during 24 hours as a function of distance from the ice front and the effects of varying thermal driving, diffusivities/ viscosity, density gradient, crystal radius, inflow velocity and simulation run time. Higher temperatures cause a decrease in the amounts of frazil deposited due to the increased frazil melt rate and, to a lesser extent, by reducing the density of the 'ambient' and therefore stabilising the inflow. At $T^*_{in} = 1$ °C there is no deposition of frazil ice (Fig. 4.10a). A higher value of K has the effect of dispersing and smoothing the frazil deposition (Fig. 4.10b). Less frazil deposits with a stronger stratification, as the frazil-seawater mixture rises at a slower rate (Fig. 4.10c). A density gradient of -10^{-3} kg m^{-4} is sufficient to stop the instability forming. By varying crystal radius it can be seen that smaller radii form frazil at a much faster rate and so the pattern of deposition is skewed towards the area just in front of the ice front (Fig. 4.10d). A larger radius results in noticeably less deposition, at a greater distance, as the frazil crystals freeze at a slower rate due to the increased surface area to volume ratio. This is in agreement with the difference observed in Fig. 4.6. A greater inflow velocity (Fig. 4.10e) provides an increase in frazil deposition due to the larger volume flux of cold water into the model domain. Greater inflow velocities also move the peak of deposition away from the ice front. To put these 'snapshot' results into context, there is a relatively uniform increase in frazil deposition with time in the baseline case (Fig. 4.10f).

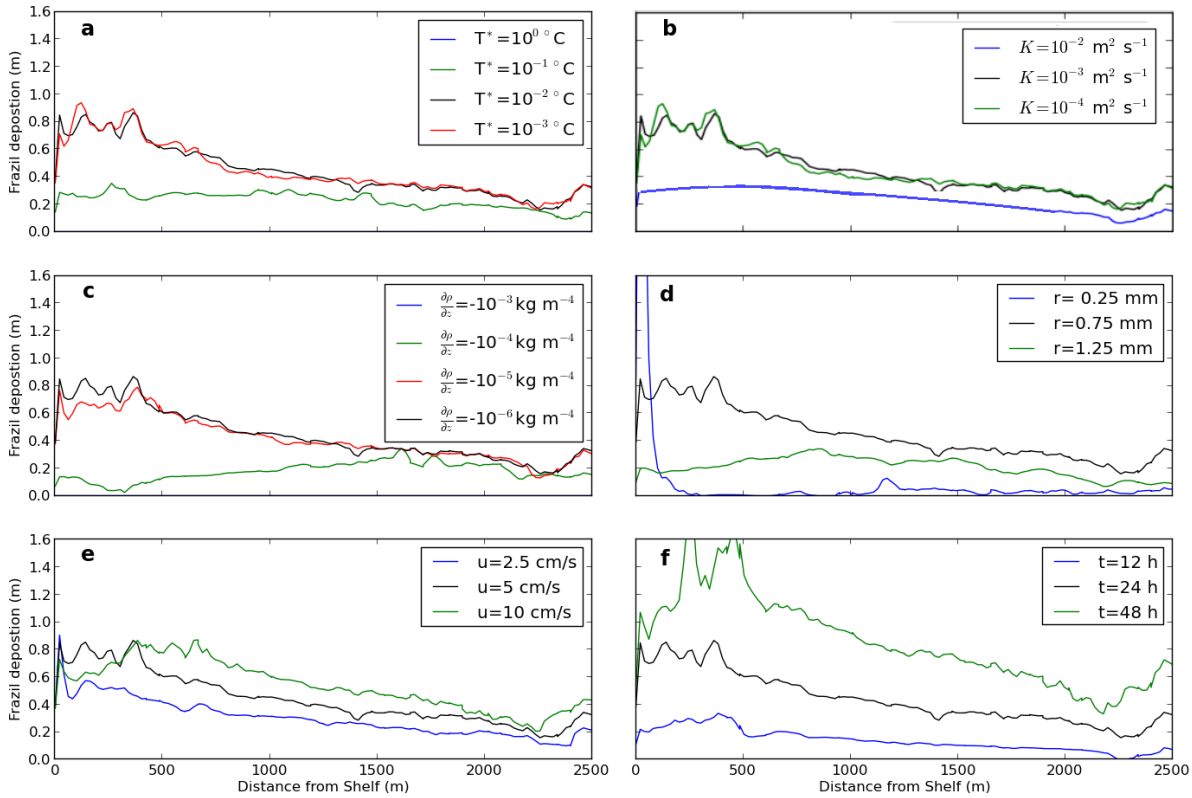

Figure 4.10: Results of the non-hydrostatic Ice Shelf Water model setup. Sensitivity of frazil ice deposition after 24 hours to (a) thermal driving, (b) background mixing, (c) stratification,fff (d) frazil crystal radius, (e) inflow velocity and (f) time. In each case the baseline case is shown in black.

The model shows that frazil ice can deposit on the underside of sea ice a significant distance from the ice front of nearby ice shelves. The instability could be a process important in the known formation of frazil ice beneath sea ice in Antarctica (*Leonard et al.*, 2006; *Mahoney et al.*, 2011). The water conditions observed by *Leonard et al.* (2006) and *Robinson et al.* (2010) fall within the bounds that the results indicate for instabilities and frazil ice growth, given an initial perturbation from an ISW plume. Given the right conditions, the ice growth rates from frazil ice growth found here are orders of magnitude greater than congelation sea ice growth.

4.4 Conclusions

The conditional frazil ice-generated instability in seawater has been investigated by firstly considering the response to an infinitesimal perturbation using a linear stability analysis, and then the full conditional stability using a non-hydrostatic ocean model. The effect of this instability upon ice growth in front of ice shelves has also been examined, and the following conclusions are drawn:

1. In a marginally gravitationally unstable water column, the frazil ice instability can co-exist with the 'background' convection. Convection becomes dominant as the 'background' temperature and salinity are more unstable.

2. The instability does not operate in the presence of strong stratification, high thermal driving (warm water), a small initial perturbation, high 'background' mixing or the prevalence of large frazil ice crystals. It is largely unmodified by frazil crystals rising relative to their surrounding water.

3. ISW plumes in reality contain a mixture of frazil ice and a freshwater anomaly, and as such the presence of a frazil ice instability can enhance an underlying freshwater anomaly-driven density perturbation. The density perturbation driving the

instability is not necessarily expressed in frazil ice at all times; an initial frazil perturbation may melt into a freshwater anomaly perturbation that drives re-growth of ice.

4. Given a large enough initial perturbation this instability could allow significant rates of ice growth.

5. The model shows significant ice growth several kilometres from an ice shelf, under similar conditions to observations of frazil ice growth under sea ice. The presence of this instability could be a factor affecting the growth of sea ice near ice shelves, with implications for AABW formation.

5 Conclusions

This thesis has investigated ice-ocean interactions in and around ice shelves using Fluidity, a finite element ocean model. In particular, the model has been used to investigate ocean dynamics and melting and freezing within ice shelf basal crevasses and the conditional instability of frazil ice growth. The overall aim of this work has been to provide a first examination of processes that are impractical to study in the field or the laboratory.

Chapter 3 presented the results of using this model to investigate ice-ocean interaction and ocean dynamics within an ice shelf basal crevasse. The circulation within a crevasse was found to be highly dependent upon the amount of freezing happening within the crevasse. Two distinct flow régimes were found, one dominated by freezing and one by meltwater. In the freezing dominated case, freezing at the top of the crevasse produces relatively denser water due to the salinity increase from brine rejection. This dense water then drives an overturning within the crevasse itself. In the meltwater driven case the less dense water rises into the crevasse, filling it. This stratifies the water column, and the crevasse has a negligible effect on the ocean flow. Freezing in the crevasse was found to be dominated by frazil ice precipitation rather than direct freezing. The key factors affecting freeze rates within basal crevasses were found to be the size of the single representative frazil crystal radius used and the amount of supercooling present within the crevasse. The amount of

supercooling has a non linear relationship with the freeze rate and as such it was thought to be unlikely that more than roughly 60 m of supercooling would exist in nature as the crevasse would quickly freeze over if this was the case. Ocean forcing was found to be insufficient to explain the widening of crevasses as they propagate towards the calving front, implying that glacial processes are required to maintain crevasses.

The presence of basal crevasse affects the stability of ice shelves, and the work presented here shows the conditions under which freezing can occur in them, thereby increasing ice shelf stability. The key factor in whether this freezing takes place is the temperature of the ocean itself. The state to which the ice shelf-ocean system tends is always one in which all supercooled water is replaced by ice. This means that cold water ice shelves, such as the Larsen and Filchner-Ronne ice shelves will be a lot more stable, as any basal crevasses that appear can be filled in with newly formed marine ice. In contrast, warm water ice shelves such as Pine Island Glacier will be unable to fill in any basal crevasse that appear and are likely to be inherently less stable as a result (though note that our results suggest that in such a situation the ocean will erode crevasses by preferentially melting ice around them.

If a changing climate were to result in a warming of the ocean under cold water ice shelves, raising the freezing point to higher than that of the top of their basal crevasses, then freezing will no longer occur in them, with a reduction in ice shelf stability.

Chapter 4 presented an investigation into the conditional instability of frazil ice. It was found that frazil ice growth caused by the rising of supercooled water was able to generate a buoyancy driven instability. However, this instability can not exist in the presence of strong stratification, high thermal driving, high background mixing, the prevalence of large frazil ice crystals or if there is a small initial perturbation.

The perturbation is largely unmodified by frazil crystals rising relative to the surrounding water. Whilst frazil ice growth generates this instability it is primarily a density perturbation; an initial frazil ice perturbation can melt into a freshwater perturbation and then refreeze. Provided there is a large enough initial perturbation this instability could be responsible for significant amounts of ice growth. Ice growth can even happen in a water column that is initially everywhere above the freezing point. Model results show significant amounts of ice growth up to several kilometres from an ice shelf. The presence of this instability could be a factor affecting the growth of sea ice near ice shelves, with implications for AABW formation.

5.1 Future Work

A key limitation of this work has been the use of a frazil ice model with a single representative size class. Sensitivity studies show that the frazil crystal radius used has significant effects upon the results. Models that assign a probability distribution to frazil crystal radius do exist (*Smedsrud and Jenkins*, 2004; *Holland and Feltham*, 2005; *Galton-Fenzi et al.*, 2012), and their use could potentially remove this element of uncertainty from the model. It is likely to significantly increase the computational expense, however.

The basal crevasse model in chapter 3 is limited to two dimensions. Expanding the model to three dimensions would allow ocean flow that is not directly across the crevasse to be modelled. The 'angle of attack' of the inflow water could have an effect on both the circulation within a crevasse and also the melting and freeze rates within the crevasse. The strength of the overturning circulation within the crevasse could be a result of the two dimensional nature of the model restricting flow in the along crevasse direction. It seems unlikely the general pattern of flow will change, as the dense water formed by freezing at the top of the crevasse will still need to

sink, but there could be spatial variation along a crevasse.

By using mesh adaptivity within Fluidity it should be possible to change the model mesh geometry in response to melting and freezing. This would allow the evolution of a crevasse with time to be investigated. Observations of crevasse's show that they tend to be triangular in shape, and it would be interesting to see if a crevasse will over time tend towards this shape.

This model has initially been used to study basal crevasses on the underside of an ice shelf, however it could easily be adapted to study other cases of ice-ocean interaction. For example, large, terrace-like features hundreds of meters wide separated by 5–50m high walls have been observed in the flanks of channels on the underside of Pine Island and Petermann glaciers (*Dutrieux et al.*, 2014). The processes leading to their formation are as yet unknown, and the model used in this work would be well suited to investigating this problem, particularly if the model were to incorporate feedback between melt rates and model mesh geometry.

Bibliography

Bamber, J. L., R. E. M. Riva, B. L. A. Vermeersen, and A. M. LeBrocq (2009), Reassessment of the Potential Sea-Level Rise from a Collapse of the West Antarctic Ice Sheet, *Science*, *324*, 901–903. 1.3.1

Bromwich, D. H., J. P. Nicolas, A. J. Monaghan, M. A. Lazzara, L. M. Keller, G. A. Weidner, and A. B. Wilson (2013), Central west antarctica among the most rapidly warming regions on earth, *Nature Geoscience*, *6*, 139–145, doi:10.1038/ngeo1671. 1.2

Bryan, K. (1962), Measurements of meridional heat transport by ocean currents, *Journal of Geophysical Research*, *67*(9), 3403–3414, doi:10.1029/JZ067i009p03403. 1.2.1

Clark, S., and J. Doering (2006), Laboratory experiments on frazil-size characteristics in a counterrotating flume, *Journal of Hydraulic Engineering*, *132*(1), 94–101, doi:10.1061/(ASCE)0733-9429(2006)132:1(94). 2.2.1, 3.4.3

Cook, A. J., and D. G. Vaughan (2010), Overview of areal changes of the ice shelves on the Antarctic Peninsula over the past 50 years, *The Cryosphere*, *4*, 77–98. 1.3.2

Daly, S. F. (1984), Evolution of frazil ice in natural water bodies, in *International Association for Hydraulic Research Working Group on Thermal Regimes: Report on Frazil Ice*, edited by S. F. Daly, pp. 19–24, US Army Cold Regions Research and Engineering Laboratory, Hanover, New Hampshire. 1.3.2, 2.2.2

Dieckmann, G., G. Rohardt, H. Hellmer, and J. Kipfstuhl (1986), The occurrence of ice platelets at 250 m depth near the filchner ice shelf and its significance for sea ice biology, *Deep Sea Research Part A. Oceanographic Research Papers*, *33*(2), 141 – 148, doi:10.1016/0198-0149(86)90114-7. 1.4, 2.2.1

Dutrieux, P., C. Stewart, A. Jenkins, K. W. Nicholls, H. F. J. Corr, E. Rignot, and K. Steffen (2014), Basal terraces on melting ice shelves, *Geophysical Research Letters*, *41*(15), 5506–5513, doi:10.1002/2014GL060618. 5.1

Foldvik, A., and T. Kvinge (1974), Conditional instability of sea water at the freezing point, *Deep Sea Research and Oceanographic Abstracts*, *21*(3), 169 – 174, doi:10.1016/0011-7471(74)90056-4. 1.6, 1.6

Foldvik, A., T. Gammelsrd, S. sterhus, E. Fahrbach, G. Rohardt, M. Schrder, K. W. Nicholls, L. Padman, and R. A. Woodgate (2004), Ice shelf water overflow and

bottom water formation in the southern Weddell Sea, *Journal of Geophysical Research: Oceans*, *109*(C2), doi:10.1029/2003JC002008. 1.3

Galton-Fenzi, B. K., J. R. Hunter, R. Coleman, S. Marsland, and R. C. Warner (2012), Modelling the basal melting and marine ice accretion of the Amery Ice Shelf, *Journal of Geophysical Research*, doi:10.1029/2012JC008214. 2.2, 5.1

Glasser, N. F., and T. A. Scambos (2008), A structural glaciological analysis of 2002 Larsen B Ice Shelf collapse, *Journal of Glaciology*, *54*, 3–16. 1.3.1

Gosink, J. P., and T. E. Osterkamp (1983), Measurements and analyses of velocity profiles and frazil ice-crystal rise velocities during periods of frazil-ice formation in rivers, *Annals of Glaciology*, *4*, 79–84. 2.2.1, 2.2.1

Griggs, J., and J. Bamber (2011), Antarctic ice-shelf thickness from satellite radar altimetry, *Journal of Glaciology*, *57*(203), 485–498, doi:doi:10.3189/002214311796905659. (document), 1.3

Hall, M. M., and H. L. Bryden (1982), Direct estimates and mechanisms of ocean heat transport, *Deep Sea Research Part A. Oceanographic Research Papers*, *29*(3), 339 – 359, doi:http://dx.doi.org/10.1016/0198-0149(82)90099-1. 1.2.1

Hattermann, T., O. A. Nst, J. M. Lilly, and L. H. Smedsrud (2012), Two years of oceanic observations below the Fimbul Ice Shelf, Antarctica, *Geophysical Research Letters*, *39*(12), n/a–n/a, doi:10.1029/2012GL051012. 3.2.1

Hellmer, H., and D. Olbers (1989), A two-dimensional model for the thermohaline circulation under an ice shelf, *Antarctic Science*, *1*, 325–336. 1.3

Hellmer, H. H., and S. S. Jacobs (1992), Ocean interactions with the base of Amery Ice Shelf, Antarctica, *Journal of Geophysical Research: Oceans*, *97*(C12), 20,305–20,317, doi:10.1029/92JC01856. 1.5

Holland, P. R., and D. L. Feltham (2005), Frazil dynamics and precipitation in a water column with depth-dependant supercooling, *Journal of Fluid Mechanics*, *530*, 101–124. (document), 1.5, 1.6, 2.1, 2.2, 2.2.2, 5.1

Holland, P. R., H. F. J. Corr, D. G. Vaughan, A. Jenkins, and P. Skvarca (2009), Marine ice in Larsen Ice Shelf, *Geophysical Research Letters*, *36*(11), doi:10.1029/2009GL038162. (document), 1.4, 1.5, 1.8

Holland, P. R., H. F. Corr, H. D. Pritchard, D. G. Vaughan, R. J. Arthern, A. Jenkins, and M. Tedesco (2011), The air content of Larsen Ice Shelf, *Geophysical Research Letters*, *38*(10), L10,503. 1.3.1

Hughes, K. G., P. J. Langhorne, G. H. Leonard, and C. L. Stevens (2014), Extension of an Ice Shelf Water plume model beneath sea ice with application in McMurdo Sound, Antarctica, *Journal of Geophysical Research: Oceans*, doi:10.1002/2013JC009411. 1.6

Humbert, A., and D. Steinhage (2011), The evolution of the western rift area of the Fimbul Ice Shelf, Antarctica, *The Cryosphere*, *5*, 931–944, doi:10.5194/tc-5-931-2011. 1.5

IPCC (Ed.) (2013), *IPCC, 2013: Climate Change 2013: The Physical Science Basis.*, Cambridge University Press, Cambridge, United Kingdom and New York, NY, USA, doi:10.1017/CBO9781107415324. 1.2

Jacobs, C. T., G. S. Collins, M. D. Piggott, S. C. Kramer, and C. R. G. Wilson (2012), Multiphase flow modelling of volcanic ash particle settling in water using adaptive unstructured meshes, *Geophysical Journal International*, doi:10.1093/gji/ggs059. 2.2.1

Jenkins, A., and A. Bombosch (1995), Modeling the effects of frazil ice crystals on the dynamics of Ice Shelf Water plumes, *Journal of Geophysical Research*, *100*, 6967–6981. 1.6, 1.7, 2, 2.1, 2.2, 2.2.2, 2.2.2, 2.2.3, 2.3

Jenkins, A., H. H. Hellmer, and D. M. Holland (2001), The role of meltwater advection in the formulation of conservative boundary conditions at an iceocean interface, *Journal of Physical Oceanography*, *31*, 285–296. 2.3

Jezek, K. C. (1984), A modified theory of bottom crevasses used as a means for measuring the buttressing effect of ice shelves on inland ice sheets, *Journal of Geophysical Research: Solid Earth*, *89*(B3), 1925–1931, doi:10.1029/JB089iB03p01925. 1.5, 1.5

Jezek, K. C., and C. R. Bentley (1983), Field studies of bottom crevasses in the Ross Ice Shelf, Antarctica, *Journal of Glaciology*, *29*, 118–129. 1.5

Jordan, J. R., P. R. Holland, A. Jenkins, M. D. Piggott, and S. Kimura (2014), Modeling ice-ocean interaction in ice-shelf crevasses, *Journal of Geophysical Research: Oceans*, *119*(2), in press, doi:10.1002/2013JC009208. (document), 1.7, 3.1, 4.2.1

Jordan, J. R., P. R. Holland, A. Jenkins, M. D. Piggott, and S. Kimura (2015), On the conditional instability of frazil ice, *Journal of Physical Oceanography*, doi:doi:10.1175/JPO-D-14-0159.1. (document), 4.1

Khazendar, A., and A. Jenkins (2003), A model of marine ice formation within Antarctic ice shelf rifts, *Journal of Geophysical Research*, *108(C7)*, 3235, doi:10.1029/2002JC001673. (document), 1.5, 1.5, 1.5, 1.7, 1.6, 3.2, 3.3

Kimura, S., A. Candy, P. Holland, M. Piggott, and A. Jenkins (2013), Adaptation of an unstructured-mesh, finite-element ocean model to the simulation of ocean circulation beneath ice shelves, *Ocean Modelling*. 2, 2.2.1, 2.3

Leonard, G. H., C. R. Purdie, P. J. Langhorne, T. G. Haskell, M. J. M. Williams, and R. D. Frew (2006), Observations of platelet ice growth and oceanographic conditions during the winter of 2003 in McMurdo Sound, Antarctica, *Journal of Geophysical Research: Oceans*, *111*(C4), doi:10.1029/2005JC002952. 1.4, 4.3.2

Luckman, A., D. Jansen, B. Kulessa, E. C. King, P. Sammonds, and D. I. Benn (2012), Basal crevasses in Larsen C Ice Shelf and implications for their global abundance, *The Cryosphere*, *6*(1), 113–123, doi:10.5194/tc-6-113-2012. 1.5, 1.5, 3.4.1

Mahoney, A. R., A. J. Gough, P. J. Langhorne, N. J. Robinson, C. L. Stevens, M. M. J. Williams, and T. G. Haskell (2011), The seasonal appearance of ice shelf water in coastal Antarctica and its effect on sea ice growth, *Journal of Geophysical Research: Oceans*, *116*(C11), doi:10.1029/2011JC007060. 1.4, 4.2.1, 4.3.2

Martin, S. (1981), Frazil ice in rivers and oceans, *Annu. rev. Fluid Mech.*, *13*, 379–397. 1.4

McFarlane, V., M. Loewen, and F. Hicks (2014), Laboratory measurements of the rise velocity of frazil ice particles, *Cold Regions Science and Technology*, *106107*(0), 120 – 130, doi:http://dx.doi.org/10.1016/j.coldregions.2014.06.009. 2.2.1, 3.4.3

McGrath, D., K. Steffen, H. Rajaram, T. Scambos, W. Abdalati, and E. Rignot (2012a), Basal crevasses on the Larsen C Ice Shelf, Antarctica: Implications for meltwater ponding and hydrofracture, *Geophysical Research Letters*, *39*(16), doi:10.1029/2012GL052413. (document), 1.5, 1.5, 1.6

McGrath, D., K. Steffen, T. Scambos, H. Rajaram, G. Casassa, and J. L. Rodriguez Lagos (2012b), Basal crevasses and associated surface crevassing on the Larsen C Ice Shelf, Antarctica, and their role in ice-shelf instability, *Annals of Glaciology*, *53*(60), 10–18, doi:doi:10.3189/2012AoG60A005. 1.5, 1.5, 3.5, 3.5.1

McGuinness, M. J., M. J. M. Williams, P. J. Langhorne, C. Purdie, and J. Crook (2009), Frazil deposition under growing sea ice, *Journal of Geophysical Research: Oceans*, *114*(C7), doi:10.1029/2007JC004414. 1.4

McPhee, M. G. (2008), *Air-Ice-Ocean Interaction*, Springer. 2.3

Nicholls, K. W., and S. Østerhus (2004), Interannual variability and ventilation timescales in the ocean cavity beneath Filchner-Ronne Ice Shelf, Antarctica, *Journal of Geophysical Research: Oceans*, *109*(C4), doi:10.1029/2003JC002149. 1.3

Nicholls, K. W., S. sterhus, K. Makinson, T. Gammelsrd, and E. Fahrbach (2009), Ice-ocean processes over the continental shelf of the southern Weddell sea, Antarctica: A review, *Reviews of Geophysics*, *47*(3), doi:10.1029/2007RG000250. 1.3

Orheim, O., J. O. Hagen, S. Østerhus, and A. C. Sactrang (1990), Glaciological and oceanographic studies on Fimbulisen during NARE 1989/90, *Filchner-Ronne Ice Shelf Programme Report*, *4*, 120–129. (document), 1.5, 1.7, 3.2, 3.2.1, 3.2

Østerhus, S., and O. Orheim (1992), Studies through Jutulgryta, Fimbulisen in the 1991/92 season, *Filchner-Ronne Ice Shelf Programme Report*, *6*, 103–109. 1.5

Parkinson, S., J. Hill, M. D. Piggott, and P. A. Allison (2014), Direct numerical simulations of particle laden currents with adaptive, discontinuous finite elements, *Geoscientific Model Development*, doi:10.5194/gmd-7-1945-2014. 2.2.1, 2.2.1

Penrose, J. D., M. Conde, and T. J. Pauly (1994), Acoustic detection of ice crystals in antarctic waters, *Journal of Geophysical Research: Oceans*, *99*(C6), 12,573–12,580, doi:10.1029/93JC03507. 1.4

Price, D., W. Rack, P. J. Langhorne, C. Haas, G. Leonard, and K. Barnsdale (2014), The sub-ice platelet layer and its influence on freeboard to thickness conversion of Antarctic sea ice, *The Cryosphere*, *8*(3), 1031–1039, doi:10.5194/tc-8-1031-2014. 1.4

Pritchard, H. D., R. J. Arthern, D. G. Vaughan, and L. A. Edwards (2009), Extensive dynamic thinning on the margins of the Greenland and Antarctic ice sheets, *Nature*, *461*, 971–975, doi:10.1038/nature08471. 1.3

Pritchard, H. D., S. R. M. Ligtenberg, H. A. Fricker, D. G. Vaughan, M. R. van den Broeke, and L. Padman (2012), Antarctic ice-sheet loss driven by basal melting of ice shelves, *Nature*, *484*, 502–505, doi:10.1038/nature10968. 1.3

Rignot, E., and D. R. MacAyeal (1998), Ice-shelf dynamics near the front of the Filchner-Ronne Ice Shelf, Antarctica, revealed by SAR interferometery, *Journal of Glaciology*, *44*, 405–418. 1.5

Rignot, E., G. Casassa, P. Gogineni, W. Krabill, A. Rivera, and R. Thomas (2004), Accelerated ice discharge from the Antarctic Peninsula following the collapse of Larsen B Ice Shelf, *Geophysical Research Letters*, *31*(18), n/a–n/a, doi:10.1029/2004GL020697. 1.3.1

Rignot, E., S. Jacobs, J. Mouginot, and B. Scheuchl (2013), Ice-Shelf melting around Antarctica, *Science*, *341*(6143), 266–270, doi:10.1126/science.1235798. 1.3

Rist, M. A., P. R. Sammonds, H. Oerter, and C. S. M. Doake (2002), Fracture of antarctic shelf ice, *Journal of Geophysical Research: Solid Earth*, *107*(B1), ECV 2–1–ECV 2–13, doi:10.1029/2000JB000058. 1.5

Robin, G. (1979), Formation, flow and disintegration of ice shelves, *J. Glaciol*, *24*, 259–271. 1.3.2

Robinson, N. J., M. J. M. Williams, P. J. Barrett, and A. R. Pyne (2010), Observations of flow and ice-ocean interaction beneath the McMurdo Ice Shelf, Antarctica, *Journal of Geophysical Research: Oceans*, *115*(C3), doi:10.1029/2008JC005255. 1.4, 2.2.1, 4.3.2

Robinson, N. J., M. J. M. Williams, C. L. Stevens, P. J. Langhorne, and T. G. Haskell (2014), Evolution of a supercooled Ice Shelf Water plume with an actively growing subice platelet matrix, *Journal of Geophysical Research: Oceans*, doi:10.1002/2013JC009399. 1.4

Scambos, T., T. Haran, M. Fahnestock, T. Painter, and J. Bohlander (2007), Modis-based mosaic of antarctica (moa) data sets: Continent-wide surface morphology and snow grain size, *Remote Sensing of Environment*, *111*(23), 242 – 257, doi:http://dx.doi.org/10.1016/j.rse.2006.12.020, remote Sensing of the Cryosphere Special Issue. (document), 1.8

Scambos, T. A., C. Hulbe, M. Fahnestock, and J. Bohlander (2000), The link between climate warming and break-up of ice shelves in the Antarctic Peninsula, *Journal of Glaciology*, *46*(154), 516–530, doi:doi:10.3189/172756500781833043. 1.3.2

Shepherd, A., D. Wingham, T. Payne, and P. Skvarca (2003), Larsen ice shelf has progressively thinned, *Science*, *302*, 856–859. 1.3.1

Shepherd, A., E. R. Ivins, G. A, V. R. Barletta, M. J. Bentley, S. Bettadpur, K. H. Briggs, D. H. Bromwich, R. Forsberg, N. Galin, M. Horwath, S. Jacobs, I. Joughin, M. A. King, J. T. M. Lenaerts, J. Li, S. R. M. Ligtenberg, A. Luckman, S. B. Luthcke, M. McMillan, R. Meister, G. Milne, J. Mouginot, A. Muir, J. P. Nicolas, J. Paden, A. J. Payne, H. Pritchard, E. Rignot, H. Rott, L. S. Srensen, T. A. Scambos, B. Scheuchl, E. J. O. Schrama, B. Smith, A. V. Sundal, J. H. van Angelen, W. J. van de Berg, M. R. van den Broeke, D. G. Vaughan, I. Velicogna, J. Wahr, P. L. Whitehouse, D. J. Wingham, D. Yi, D. Young, and H. J. Zwally (2012), A reconciled estimate of ice-sheet mass balance, *Science*, *338*(6111), 1183–1189, doi:10.1126/science.1228102. 1.3

Sievers, J., A. Grindel, and W. Meier (1989), Digital satellite image mapping of Antarctica, *Polarforschung*, *59*, 25–33. (document), 1.8

Smedsrud, L. H., and A. Jenkins (2004), Frazil ice formation in an Ice Shelf Water plume, *Journal of Geophysical Research: Oceans*, *109*(C3), doi:10.1029/2003JC001851. 2.2, 5.1

Smetacek, V., R. Scharek, L. I. Gordon, H. Eicken, E. Fahrbach, G. Rohardt, and S. Moore (1992), Early spring phytoplankton blooms in ice platelet layers of the southern Weddell Sea, Antarctica, *Deep Sea Research Part A. Oceanographic Research Papers*, *39*(2), 153 – 168. 1.4

Swithinbank, C. (1977), Glaciological research in the antarctic peninsula, *Philosophical Transactions of the Royal Society of London. B, Biological Sciences*, *279*(963), 161–183, doi:10.1098/rstb.1977.0080. 1.5

Vaughan, D. G., and C. S. M. Doake (1996), Recent atmospheric warming and retreat of ice shelves on the Antarctic Peninsula, *Nature*, *379*, 328–331. 1.3

Ye, S. Q., J. Doering, and H. T. Shen (2004), A laboratory study of frazil evolution in a counter-rotating flume, *Canadian Journal of Civil Engineering*, *31*, 899–914, doi:10.1139/L04-056. 2.2.1, 3.4.3